SPIN-FILTERED TUNNELING DEVICE USING A TOPOLOGICAL INSULATOR

A Thesis

Submitted to the Graduate School

of the University of Notre Dame

in Partial Fulfillment of the Requirements

for the Degree of

Master of Science in Electrical Engineering

by

Jose R. Berlioz

_____

Christopher Hinkle, Director

Graduate Program in Electrical Engineering

Notre Dame, Indiana

April 2021

SPIN-FILTERED TUNNELING DEVICE USING A TOPOLOGICAL INSULATOR

Abstract

by

Jose. R. Berlioz

There has been much interest in the study of topological insulators (TI) recently. Due to their unique electronic structure, these new materials have been an active area of research to discover new quantum phenomena and their application in new technologies. Unlike the electronic structure observed in traditional semiconductors, the strong spin-orbit coupling induces a band inversion in the electronic structure of TIs. One of the side effects of this band inversion is creating metallic-like surface states at the material's surface that are protected by time invariance and whose spin angular momentum is locked to the direction of the momentum of the electron.

These surface states are essentially resistant to scattering events that otherwise affect other materials. Leveraging the characteristic scattering resistance, the spin-momentum locking of the surface states, and the Dirac cone structure, a spin-resonant tunneling diode using topological insulators has been investigated to implement a negative differential resistance device. Utilizing the spin texture of the surface states, an additional spin-filter can help to suppress the valley current in a negative differential resistance device. In the spin-resonant tunneling diode, the tunneling process would also

benefit from having protection from conventional scattering processes due to defects and thickness or line edge roughness.

This research is focused on the manufacturing of a spin-filtered tunnel diode. Using molecular beam epitaxy to grow a three-layer heterostructure, with two layers of bismuth selenide as the topological insulator separated by a thin layer of tungsten diselenide as a tunnel barrier. The alignment of the Fermi levels of the topological insulator layers and the thickness of the tunnel barrier were investigated using X-ray Photoelectron Spectroscopy. The fabrication and initial electrical measurements of the spin-filtered tunnel diode were also investigated.

This thesis is dedicated to my friends and family for providing support during difficult COVID times.

CONTENTS

FIGURES

ACKNOWLEDGMENTS

I would like to acknowledge and thank my advisor, Prof. Christopher Hinkle, for letting me work on this project and providing helpful guidance throughout. To Professor Seabaugh for spending valuable time to train me in the electrical characterization of my devices. To the thesis committee members who took time off their busy schedule to evaluate my topic.

I would also like to thank the National Science Foundation for their generous grant (Award Number 1917025) which funded this research project.

Furthermore, I want to thank my research lab colleagues at the Hinkle Lab (Tian Sun and Rehan Younas) and especially to the postdoc Guanyu for providing support and advice through this project.

I thank my family and friends for supporting me through my two years of graduate school.

To my partner, Grace Hasken, who cheered me on until the date of publication.

CHAPTER 1:

INTRODUCTION

Lately, thanks to Moore's Law, the semiconductor industry has been capable of doubling the number of transistors on a chip every 1.5 years. This modern feat in scalability has come with a price as energy consumption per chip has been negatively impacted. As transistor densities scale-up and the device dimensions scale down, the exponential growth in static and dynamic power consumption of today's CMOS transistors has become a problem in need of innovative solutions [1]. New CMOS geometries like the FinFET and the adoption of high-k dielectrics are examples of innovation that enabled the scaling of CMOS devices further. However, even more exotic solutions may be required if Moore's law is to survive in the upcoming years.

One of the alternatives proposed to replace CMOS transistors are neuromorphic circuits. Neuromorphic computing is inspired by biology's efficient and compact design of the nervous system. The human brain can do an immense number of logical operations efficiently, consuming only 20 W of power while utilizing a considerably small space [2], [3]. To put this number in perspective, to beat the best Go players in 2016, DeepMind's distributed computing hardware required 1202 CPUs, and 176 GPUs of computing power [4]. Assuming each CPU and GPU consumed 300 W each, AlphaGo required an estimated 380 kW of power or the power of twenty-thousand human players. Today's

technology offers us a higher level of precision and speed in processing. Still, there is no doubt that it does not match neuromorphic structures in power efficiency and compactness in complex computational areas. Investigating these neuromorphic circuits could be the key to obtaining greater efficiency in energy consumption of specific, yet key, computation areas.

Nonlinear oscillators are the fundamental elements of neuromorphic networks, and a large number of them would be used at the nanoscale to develop the system [2], [3]. It has been known that an electrical component showing negative differential resistance (NDR) can be used in conjunction with a clocked power supply to create stable NDR devices for a neuromorphic bidimensional matrix. However, many of these nanoscale NDR devices are plagued by uniformity and reproducibility problems due to defects and imperfections [5]. This issue will be amplified by putting millions of devices in a neuromorphic system's bidimensional matrix.

By miniaturizing the transistor and entering the nanoscale realm, atomic defects have become increasingly relevant to all devices. Multiple advances have managed to perfect the crystallinity and purity of semiconductor materials and reduced the number of defects substantially [6], [7], but ultimately, materials will never be defect-free. This fact becomes pertinent when nanoscale devices' reproducibility and uniformity are expected of millions of devices working together.

The solution to this problem could lie in working with materials that are immune to defects and impurities with a higher level of effectiveness than the modern materials used. For this reason, working with materials, say, whose electronic transport is protected

from these defects and impurities by the laws of physics such as topological materials, can find tremendous success in obtaining the necessary reproducibility and uniformity.

1.1 Overview

This research focuses on the creation of a topological insulator-based NDR device. Molecular beam epitaxy was used to grow a spin-filtered tunneling heterostructure made of two topological insulators separated by a thin 2-D tunnel barrier. The topological insulator's growth and band alignment, characterization of each layer, and initial electrical characterization of the device were investigated.

The device utilizes the spin-momentum locking of a topological insulator's surface states to spin-filter the electrons tunneling from one Bi_2Se_3 film to another through a 2D tunnel barrier made out of 2D films of WSe_2 of various thicknesses.

1.2 Background on Topological Insulators

In recent years, topological insulators (TIs) have been the subject of intense study by materials and physics research groups due to their intrinsic novel quantum phenomena. Predicted in 2005 by Kane and Mele as an extension of 2-D quantum hall systems, TIs exhibit metallic states at their surface while remaining nonconducting at their bulk. These metallic states are due to the band inversion caused by these materials' spin-orbit interaction [8]. Figure 1.1 shows the basic electronic structure expected from a topological insulator. Like a typical semiconductor, the material electronic structure contains a valence band (BVB) and a conduction band (BCB) separated by a bulk gap; however, unlike ordinary materials, the bulk gap contains spin-momentum locked

topological surface states (TSS) that connect the conduction and valence bands. The metallic surface states of topological insulators have several interesting characteristics, such as time-reversal symmetry and spin-momentum locking, which result in the diminished ability of the surface states to backscatter, leading to ballistic transport[8], [9].

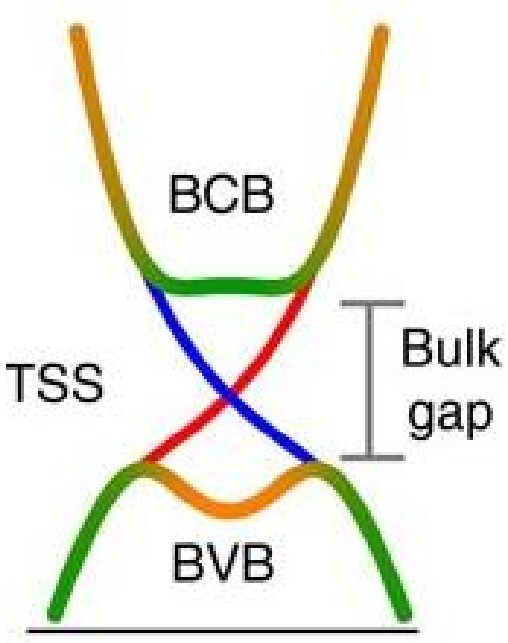

Figure 1.1 - Simplified diagram of the electronic structure of a topological insulator [10].

In practical terms, this means that the surface states are resistant to being disturbed by outside influences such as defects or surface roughness. As long as the spin degeneracy is maintained, the surface/edge state electrons have their spin and momentum locked and exhibit significantly diminished scattering. Even though spin-flipping scattering processes exist (e.g., hyperfine interactions), they are typically orders of magnitude weaker than conventional (protected) scattering. Carriers through these surface states are spin-polarized, and they have incredibly high electron mobility.

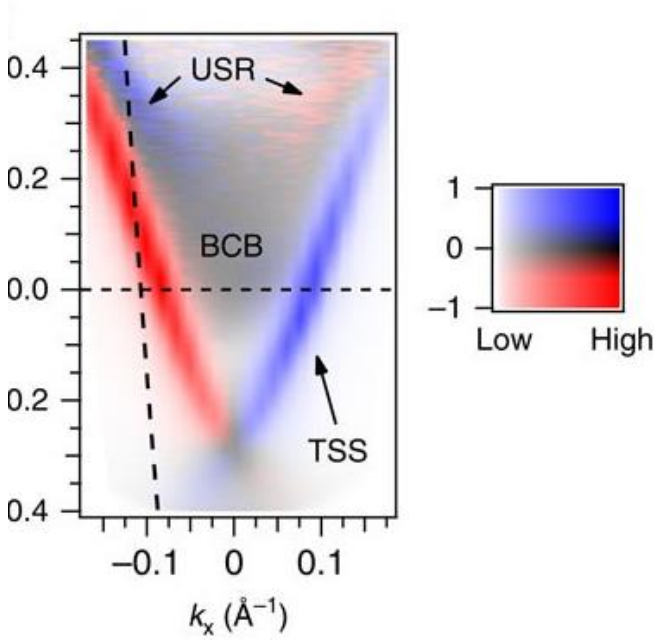

Figure 1.2 - Spin-resolved ARPES measurement of Bi_2Se_3 [10].

Advances in photoemission technology, like angle-resolved photoemission spectroscopy (ARPES), have given us a detailed view into the electronic structure of modern topological materials. By illuminating the sample, usually with either a UV plasma source or a synchrotron light source and measuring the intensity and angle of the electrons' photoemission, ARPES can probe the density of states and the momentum of the sample. With ARPES, the Dirac cones associated with the inverted bandgap predicted in these materials have been experimentally verified [11]. Recently the inclusion of spin-resolved measurements for angle-resolved photoemission spectroscopy (ARPES) has proven even further the spin-momentum locking of these materials.

Figure 1.2 shows the recent spin-resolved ARPES measurements done by C. Jozwiak [10] on Bi_2Se_3. Bi_2Se_3 is a topological insulator of most interest for developing the NDR device since it has a relatively simple electronic band structure with a single Dirac cone and a relatively large bulk bandgap of ~0.3 eV, which allows for the topological insulator behavior to be observed at room temperature. These features, along with the recent advancements in the ease of n-type doping of Bi_2Se_3, through selenium vacancies, and having an excellent growth interface with WSe_2, will be exploited in the device for tuning the Fermi level and creating a sharp junction.

1.3 Device Physics

The transport behavior of tunneling electrons from Bi_2Se_3 films through a 0.5 nm vacuum was calculated by collaborator Prof. William Vandenberghe using a Bardeen transfer Hamiltonian and is shown in Fig 1.3. The model gives us an understanding of the device physics expected on the experimental results. The Fermi levels of the two films were designed to be different by 0.1 eV to observe the effect; it is required that the Fermi levels are not in the conduction band and that they be different from each other. This will be important later on when Fermi level tuning is examined.

Furthermore, with respect to the tunnel barrier, to observe tunneling between the films, careful control of the tunnel barrier's thickness is needed. The tunnel barrier should not be thick enough to prohibit tunneling and not too thin to become leaky. To explore the effects of WSe_2 thickness on the transport behavior of the tunneling diode, 4 films were grown with different growth times:

- Sample 1 was grown for 3 hours

- Sample 2 was grown for 5 hours
- Sample 3 was grown for 7 hours
- Sample 4 was grown for 9 hours

Thickness estimations of each sample using XPS are done in Section 2.3.3.

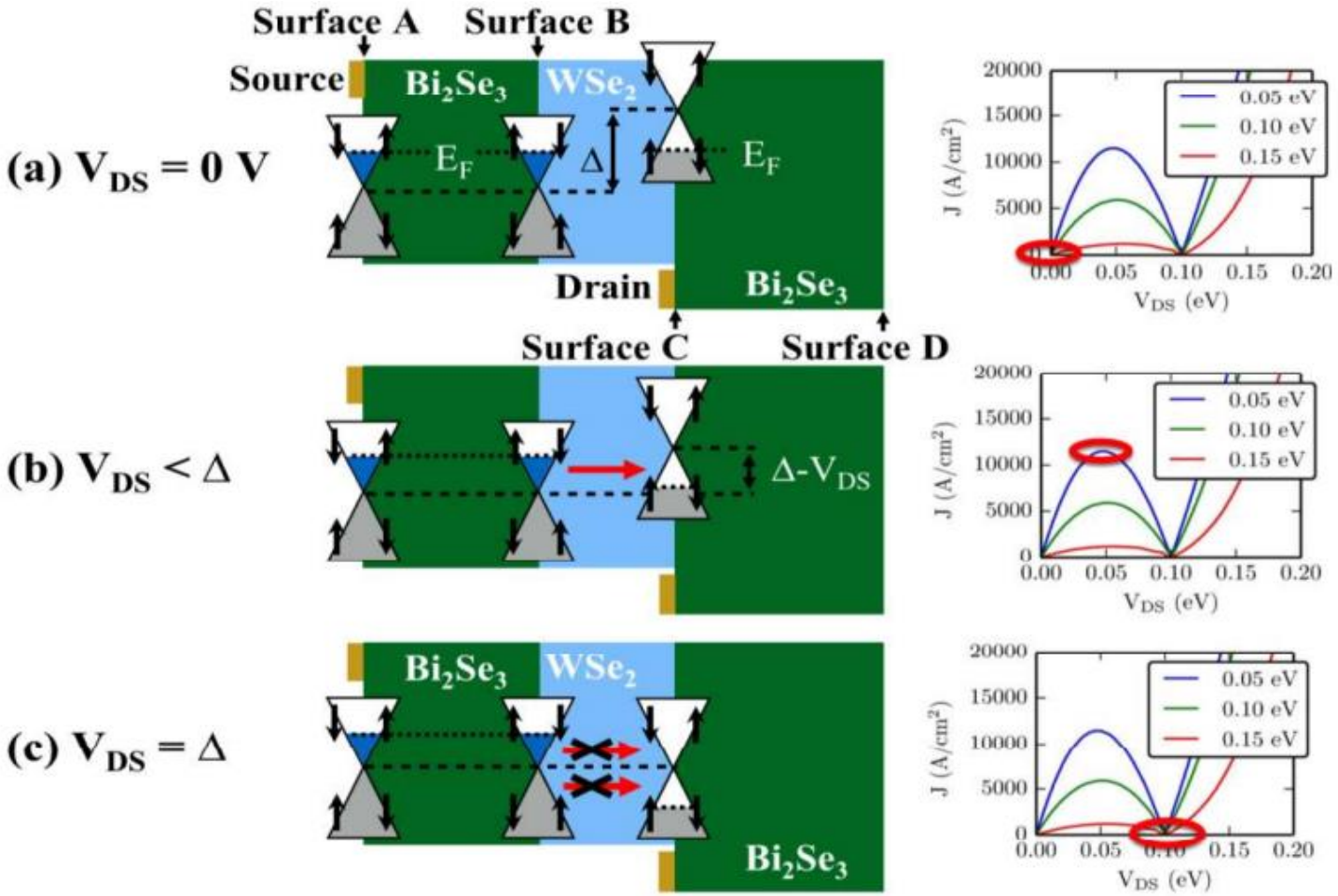

Figure 1.3 - Schematic diagrams of the proposed two-terminal $Bi_2Se_3/WSe_2/Bi_2Se_3$ heterostructure and the Dirac cones' alignment at important bias conditions.

Figure 1.3 illustrates the way this two-terminal device will work. Tunneling occurs between the sections of the Dirac cone with the same spin from surface B to surface C. Figure 1.3 (a) shows the Dirac cones' initial misalignment due to the different doping levels of the Bi_2Se_3 films. No current should flow due to the system being in equilibrium ($V_{DS} = 0$ V). Current begins to increase as we apply a small bias voltage in Figure 1.3 (b), the Dirac cones shift relative to each other, and electrons can tunnel between the conduction band of surface B to the valence band of surface C (which have the same spin texture). Further increase in voltage to V_{DS} causes the alignment of the Dirac cones (panel c), and the current drops to zero as tunneling is prohibited due to spin filtering. Despite the complete alignment, which opens a maximum of states that conserve both energy and momentum, the spin is opposite and the requirement of conservation of spin for tunneling is not met.

The numerical calculations show that the current vanishes as the Dirac cones align with each other. Still, the expected behavior is that there will be some current present due to parasitics. Unlike conventional resonant tunneling diodes though, these parasitics should be diminished due to the topological protection and should not largely degrade the tunneling.

Another important note is that surfaces A and D have the same spin as surfaces C and B, respectively. These same spin surfaces are also available for tunneling, especially when the Dirac cones align, eliminating the desired spin-filtering to suppress the valley current. However, this is easily solved by increasing the thickness of the Bi_2Se_3 layers; this must be done anyways, as the film thickness needs to be greater than 6 QLs (6 nm) or deterioration of the Dirac cones will be observed [12].

1.4 Photoemission Spectroscopy Fundamentals

Photoemission spectroscopy (PES) is an excellent tool for determining a material's chemistry and band structure and was used extensively along with RHEED. The versatility and importance of X-ray-Photoemission Spectroscopy (XPS) for this research cannot be underestimated as it was used to obtain the position of the Fermi level of each Bi_2Se_3 film, to detect sources of contamination with >1% concentration in the films, to assess the quality of the growth, and finally to measure the thickness of the WSe_2 layer with nanometric accuracy. For that reason, a brief section on the fundamentals of XPS is included.

X-ray photoemission spectroscopy uses an Al anode as a photon source to create a monochromatic beam in the x-ray energy range. The technique uses the photoelectric effect to probe the electronic density of states up to the Fermi edge of the top layers of a material. It has a photoelectron escape depth dependent on the material properties, but it is estimated to be around 10 nm for most materials. As the x-ray beam hits the target, electrons are excited from their current energy levels and emitted out of the material. The emitted electrons go through a hemispherical analyzer where their kinetic energy is recorded. Figure 1.4 shows a simplified schematic of the photoemission process in XPS.

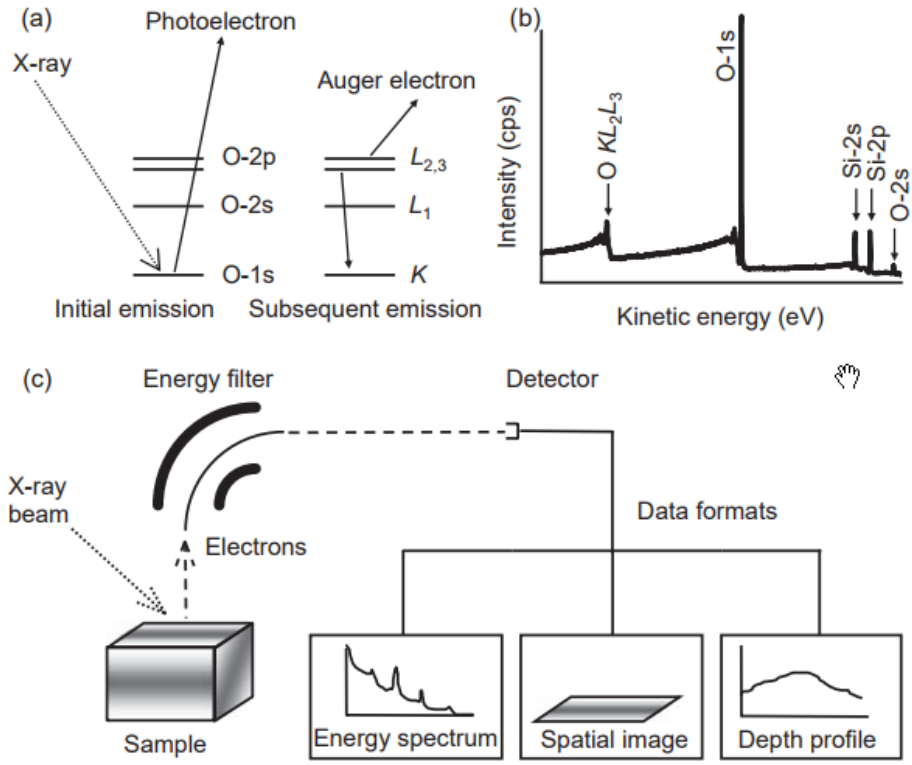

Figure 1.4 - Simplified schematic of X-ray Photoemission. (a) Shows the types of emission expected. (b) Shows a typical XPS spectrum. The XPS spectrum contains peaks that translate to information about the binding energies of electrons in the sample. (c) Shows the path taken by the photoemitted electrons. Electrons pass through the energy filter, arrive at the detector, and are digitized to different data formats [13]. With copyright permission from © 2011, John Wiley and Sons

The expected kinetic energy (KE) of the electrons observed by the analyzer can be described using Einstein's equation stated as:

$$E_B = hv - KE \tag{1.1}$$

Where E_B is the binding energy of the electron in the atom, and hv is the energy of the x-ray source. The electron's binding energy requires further elaboration as it is a function of the type of atom and its environment. Using Koopman's theorem, one can

describe the binding energy as the difference between the initial and final electron states in the following way:

$$E_B = E_f(n-1) - E_i(n) \tag{1.2}$$

Where $E_f(n-1)$ is the final energy state of the electron configuration and $E_i(n)$ is the initial energy of the electron configuration. Deviations of the binding energy observed in the XPS spectrum from what would have been an ideal energy spectrum of the elemental atomic orbitals offer us rich information on the electron configurations being examined since they correspond with changes of the initial and final electronic energy configuration. As an example, Figure 1.5 shows the effects different types of chemical bonding have on the Bi $4f_{7/2}$ peak's binding energy compared to the elemental binding energy. These observed differences to the photoemission spectrum allow XPS to provide helpful information about materials like:

- Elemental identification and quantification of any element from Li to U as long as a >0.05% atomic concentration exists.
- Reveal each element's chemical environment and bonding through analysis.
- Elemental depth profiling of the outermost 10 nm using non-destructive methods like angle-resolved XPS and photoelectrons with different escape depths.
- Elemental depth profiling several hundred of nanometers into the sample using destructive methods like ion etching.

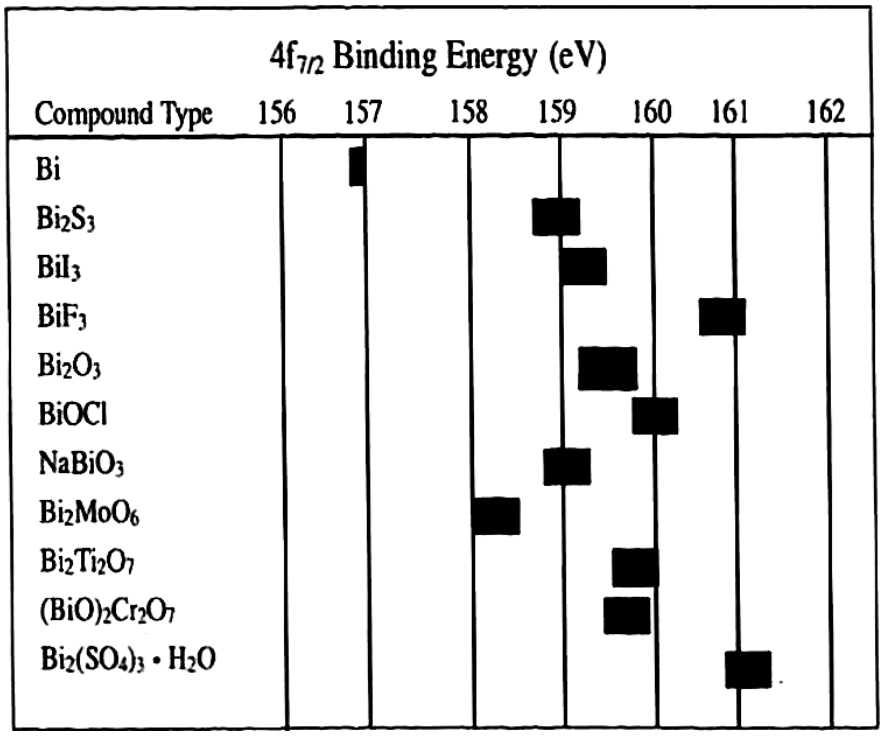

Figure 1.5 - Photoemission peak location for Bi $4f_{7/2}$ for different chemical bonds. Different chemical bonds have different binding energy locations [14]. With copyright permission from © 2011, John Wiley and Sons

1.5 Thesis Organization:

This thesis pertains to the fabrication and device characterization of a spin-filtered tunneling device. For that purpose, the thesis contains two main experimental chapters. Chapter 2 will cover each layer's growth and tuning, the growth parameters used, and the films' characterization. Chapter 3 describes the device's fabrication process and discusses the electrical characterization of the heterostructures fabricated. Finally, Chapter 4 discusses the results and points to work further required to make tunnel devices with topological insulators.

CHAPTER 2:

HETEROSTRUCTURE GROWTH AND TUNING

Let's briefly reiterate from the Bardeen Hamiltonian model in Chapter 1. To observe the device's negative differential characteristic, the device must have two things concerning the Fermi level of the bismuth selenide:

1) The Fermi levels must be within the bulk bandgap.
2) The Fermi levels of the two Bi_2Se_3 films cannot be in the same position.

We will address the first issue in the next section and the second issue in the Fermi level tuning section of Bi_2Se_3.

2.1 Molecular Beam Epitaxy Growth

If the Fermi level is in either of the bulk bands, the negative differential resistance effect will not observe as those bulk states do not have the spin-momentum locked properties which will prevent the desired spin-filtering. Selenium vacancies have been found to be the primary source of severe n-type doping in bismuth selenide films that moves E_F into the bulk conduction band and are characteristic of poorly grown films [15], [16], [17], [18]. High-quality bismuth selenide films not only have a mid-gap Fermi level, but are also more resistant to atmosphere-induced oxidation than low-quality growths and are therefore highly desirable for further fabrication steps [17].

The bismuth selenide films were grown in a Molecular Beam Epitaxy (MBE) system made by Scienta Omicron to achieve high-quality crystal growth. MBE is well-known to provide superior quality materials, as evidenced by the highest electron mobilities ever measured being those in an MBE-grown GaAs/AlGaAs heterostructure[7]. Figure 2.1 shows the basic anatomy of an MBE system. Effusion cells are used to deposit the material onto a rotating substrate using temperature-dependent evaporation under ultra-high vacuum conditions (10^{-8} - 10^{-12} mbar). The effusion cells contain a crucible and a heating filament made from tantalum to raise the material's temperature. The desired temperature is controlled through a PID controller that controls (as seen on Figure 2.2) the power being delivered by the filament to the crucible from the power supply.

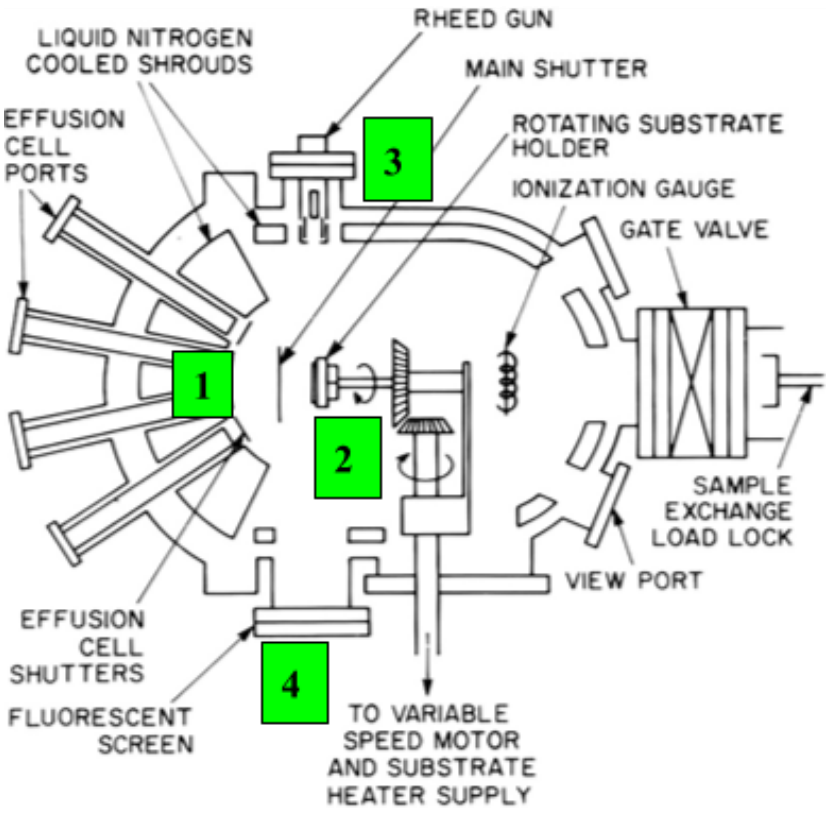

Figure 2.1 - Basic Diagram of a Molecular Beam Epitaxy System. (1) Effusion cells are used to heat ultra-high purity material sources. (2) Sample Holder contains the substrate used to grow the films, which is rotated to enforce film uniformity and be heated to adequate growth temperatures. (3) The RHEED gun is used for live in-situ surface characterization of the film using an electron beam diffraction pattern. (4) The fluorescent screen made with a phosphor-coated film displays the diffraction pattern. Reprinted from [19] with the permission of AIP Publishing.

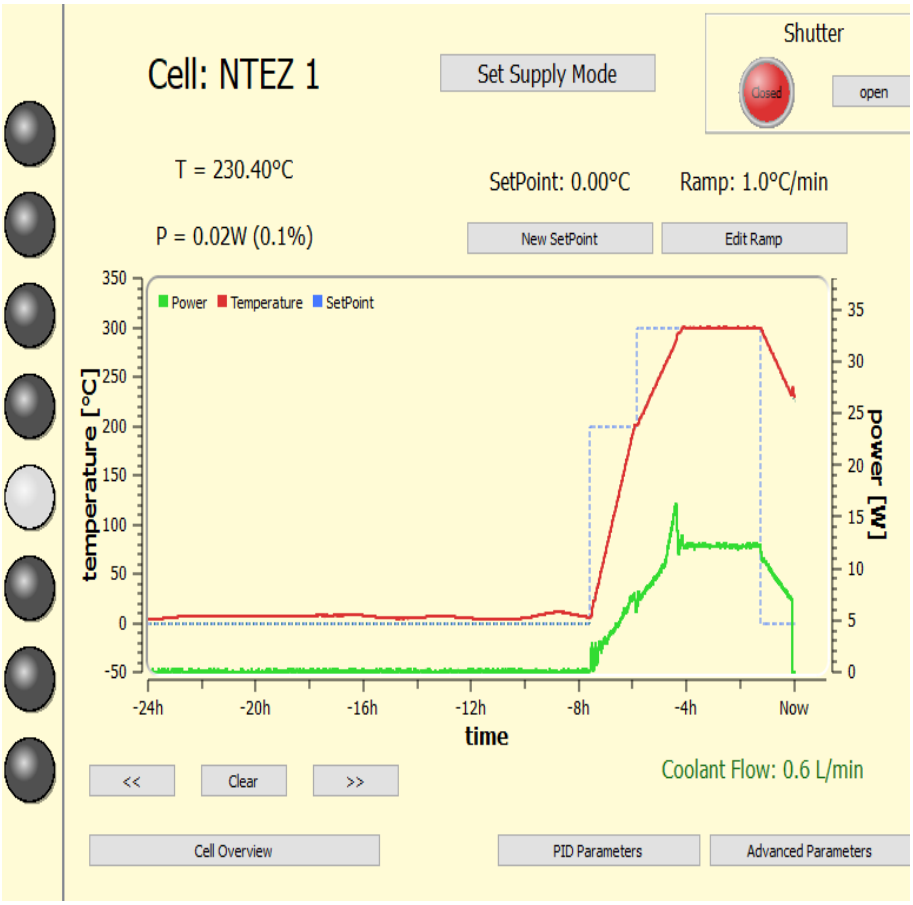

Figure 2.2 - Graphical Interface of the PID Controller controlling the Bismuth NTEZ cell.

More specific to the chamber and these experiments, Figure 2.3 shows the MBE system inside Stinson Remick's cleanroom used to grow and characterize the film growth. In conjunction with the Transition Metal Dichalgonide Chamber (TMDC) where the films were grown, the Scienta Omicron MBE system also has an in-situ XPS characterization tool and dedicated oxide and ALD chambers for other projects. Transfers between each of the chambers pass through the radial distribution chamber (UFO) and are done under an ultra-high vacuum of $1x10^{-9}$ mbar, while in-situ characterization is usually done at $1x10^{-9}$ mbar.

Figure 2.3 - Blueprints of the molecular beam epitaxy system in Stinson Remick's cleanroom. Film growth is done in TMDC EVO.

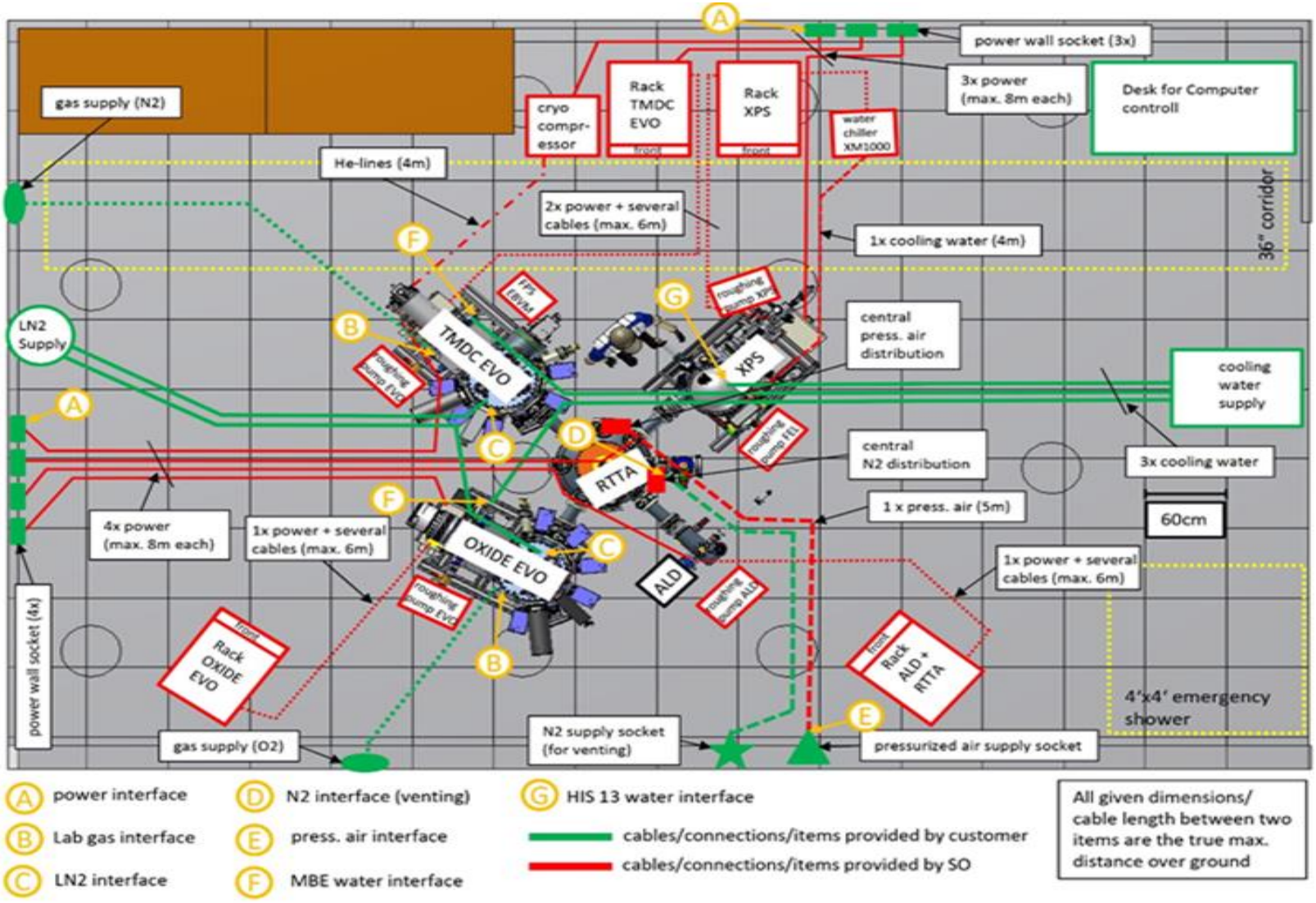
power wall socket (3x)
3x power (max. 8m each)
Desk for Computer controll
gas supply (N2)
cryo compr-essor
Rack TMDC EVO
front
Rack XPS
front
water chiller XM1000
He-lines (4m)
2x power + several cables (max. 6m)
1x cooling water (4m)
36" corridor
LN2 Supply
TMDC EVO
XPS
central press. air distribution
cooling water supply
RTTA
central N2 distribution
3x cooling water
1 x press. air (5m)
60cm
4x power (max. 8m each)
1x power + several cables (max. 6m)
OXIDE EVO
ALD
1x power + several cables (max. 6m)
power wall socket (4x)
Rack OXIDE EVO
front
Rack ALD + RTTA
front
4'x4' emergency shower
gas supply (O2)
N2 supply socket (for venting)
pressurized air supply socket
A power interface
B Lab gas interface
C LN2 interface
D N2 interface (venting)
E press. air interface
F MBE water interface
G HIS 13 water interface
cables/connections/items provided by customer
cables/connections/items provided by SO
All given dimensions/ cable length between two items are the true max. distance over ground

Cryo-Plex 8 Trillium cryopump that can achieve 10^{-12} mbar. During the time of the growths, the chamber had three NTEZ low-temperature effusion cells (for Se, Bi, and Zn), one WEZ standard effusion cell (for Ga), one Thermal Cracker Cell (for Se), one HTEZ (for Fe), one plasma gun (for N plasma), and an e-beam evaporator system (for W, Mo, Zr, and V). During the growths, the NTEZ effusion cells for bismuth and selenium deposition were initially used, but later a thermal cracker cell (TCC) was used for Se instead of the NTEZ cell. The TCC showed a slight improvement in the quality and consistency of the films as the second thermal cracking zone increases the reactivity of the Se flux by breaking up the atomic clusters that are present in the sublimation of Se.

As magnetic impurities break time-reversal symmetry, one primary source of worry in this research was that iron from the HTEZ cell would be introduced in the films as a contamination source. Iron doping of Bi_2Se_3 opens a gap in the Dirac cone and must be avoided for the proper operation of the proposed device. Careful coordination was needed to avoid sequential growths of iron-doped materials and Bi_2Se_3 films and prevent reutilization of the same sample holders. Moreover, the manipulator was baked for 3 hours at 900 °C between each growth, and XPS of the material was analyzed to show that there was no Fe contamination in the films, at least to the detection limit of XPS (< 1 %). Previous results with iron-doped Bi_2Se_3 show that significant deposition of iron is needed to break time-reversal symmetry, and shows the XPS analysis is enough to guarantee a standard Dirac cone[19].

2.2 Growth of Bismuth Selenide

2.2.1 Substrate

Even though lattice matching solely between layered materials is not as important compared to 3D materials, the quality of the bottom Bi_2Se_3 growth will be influenced by the choice of substrate. In 3D materials, the dangling bonds of the substrates interact with the epilayer and cause strain as the in-plane bonds are stretched or compressed. In 2D on 2D growth, these strains are relaxed and allow for a significant reduction in the requirement for lattice matching. However, this is not the scenario for a 2D material on a 3D material which is the scenario presented with the bottom Bi_2Se_3 layer growth. Any interaction between the initial Bi_2Se_3 QL layers and the substrate's dangling bonds will cause strain. For that reason, a careful selection of substrate is needed for the bottom layer.

Initial growths were performed on sapphire using the recipe by Walsh [15]. Sapphire has been shown to be an excellent substrate for Bi_2Se_3 MBE growths due to the high-quality substrates available and the inertness of the substrate. However, even though the bismuth selenide films' growths on sapphire were successful and showed sharp RHEED patterns and intrinsic Fermi levels, the fabrication of the films was difficult, as will be explained later. For fabrication and characterization reasons, a similar quality growth as described by Bansal [16] was used since it allowed us to use a conductive substrate. Bansal showed high-quality Bismuth Selenide growths on Si (111) by using a short selenium passivation step for the silicon dangling bonds at the beginning of the growth. Compared to Bansal's growths, where undoped silicon (111) was used, highly-doped n-type Si (111) was used here to enable device fabrication. Due to the low growth

temperature (220 °C), no arsenic diffusion from the substrate into the film was expected. XPS characterization of the film confirmed no contamination of arsenic.

Having a conductive substrate served in two ways. One, since XPS was utilized to characterize the Fermi level to less than 0.3 eV, a conductive substrate allowed for the avoidance of any charge compensation or ex-situ modifications to the film that would have been present if growth had been done on an insulating substrate. Second, the conductive substrate offered a native bottom contact and simplified the fabrication process. The native bottom contact minimizes the amount of processing done to the layers, and further maintains the Fermi levels measured for later analysis.

Bansal 's recipe for Si (111) required another modification as the RHEED pattern obtained was as good as Bansal 's, yet the Fermi level as measured by XPS was into the conduction band, indicating a presence of excessive Se vacancies. For that reason, the Se cell in the recipe was replaced by a cracker cell to incorporate Se into the films better [17] and increased the growth temperature to 220 °C compared to Bansal's 150 °C.

2.2.2 Bismuth Selenide Growth Parameters

Pretreatment of the Si (111) substrates involved a full RCA clean for each sample and applied a final HF dip to etch the native oxide. All samples were placed in the load lock under UHV immediately after. A pre-anneal of 400 °C for 2 minutes was used to break the hydrogen bonds with the silicon.

The final two-step growth process of each Bi_2Se_3 film is shown in the process flowchart of Figure 2.4. Both films were grown through the same approach. For the sources' growth parameters, the Bi source was kept at 490 °C, while the Se TCC was kept at 185 °C at its reservoir and 1000 °C at its cracker during both growth and anneal. The

two anneal steps were done to increase the uniformity between the films. The anneals are essential steps to keep the Fermi level position variation within less than 0.02 eV in the samples. Moreover, the final anneal step was done to increase the RHEED intensity of the first layer's growth before the WSe_2 layer and improve the interface between them. Finally, to assure that there were no human errors in terms of timing, the growth was controlled by a script using Scienta Omicron's proprietary language to automate shutters' opening and closing and substrate and source temperatures.

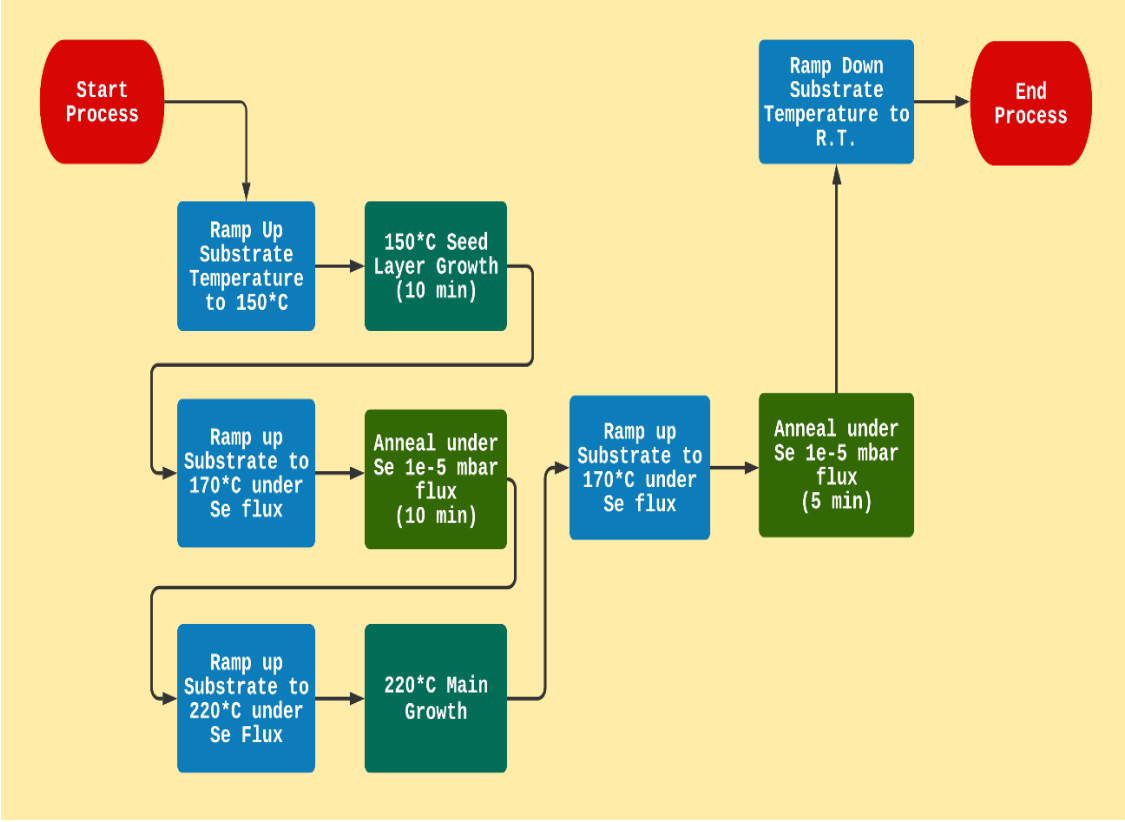

Figure 2.4 - Bi_2Se_3 Growth Flowchart. Blocks that are near the bottom are done at higher temperatures.

The growth starts after the silicon substrate's pre-anneal at 400 °C, after which the substrate is ramped down to the seed layer temperature of 150 °C. The growth begins after the Se shutter opens to passivate the surface. Three seconds later, the bismuth shutter opens as well, and the seed layer growth begins. After 10 minutes, the seed layer step ends, and the bismuth shutter is closed, leaving only the Se source. At this point, the substrate is ramped up to 170 °C under Se pressure and annealed for 10 minutes. Once the seed layer anneal is done, the substrate is ramped up once again under Se pressure until the main growth temperature of 220 °C. The main growth starts once the bismuth shutter opens. The main growth lasts between 30 minutes for the bottom layer for a total thickness of ~25 nm and 60 minutes for the top layer for ~50 nm as measured by profilometer and ellipsometry. Once the timer finishes, the bismuth shutter closes to interrupt the growth, and the substrate temperature is ramped down under Se pressure to 170 °C, where it is annealed once more for 10 minutes. The substrate is ramped down once more to 160 °C under Se pressure, at which point the Se shutter closes as not to cover the surface with selenium which starts to stick to the substrate in an amorphous layer around 150 °C. With the Se shutter closed, the substrate ramps down to room temperature.

The result of the process can be seen in Figure 2.5. The RHEED pattern is for Bi_2Se_3 along the [1 0 -1 0] direction, and it shows a sharp, streaky pattern indicative of a flat, crystalline film.

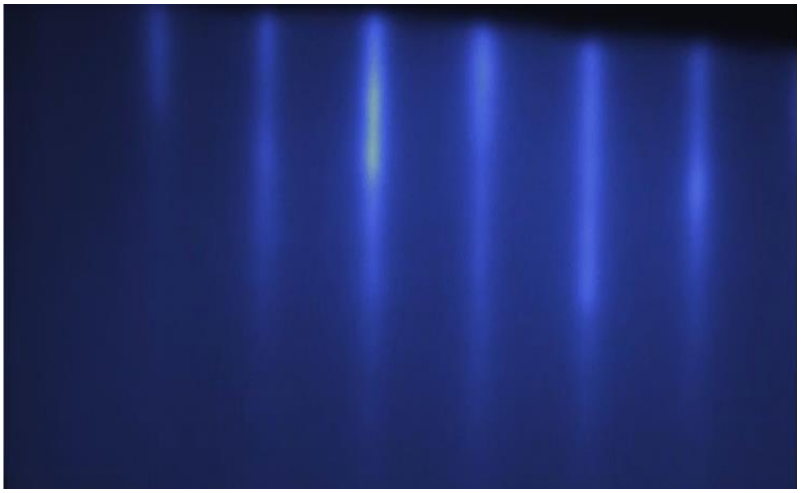

Figure 2.5 - RHEED pattern for Bi_2Se_3 along the [1,0,-1,0] direction shows a sharp, streaky pattern indicating a flat, crystalline film.

2.2.3 Fermi Level Tuning

Achieving high-quality growth was possible using this setup. To achieve Fermi level tuning using intrinsic defects Walsh's technique was utilized [15] to anneal the samples and obtain a larger amount of selenium vacancies, essentially controllably n-type doping the film.

The as-grown bottom layer achieved a Fermi level of 0.06-0.08 eV above the bulk valence band edge, which shows the crystal growth's uniformity between samples. Since the top layer reaches a similar Fermi level position as the bottom layer, the levels had to be tuned away from each other using a UHV anneal to allow for the NDR effect. Since one cannot anneal the top layer without heating the bottom layer, the bottom layer was annealed after growth to promote Se vacancies, n-type dope the film, and move E_F toward the bulk conduction band. Figure 2.6 shows UHV annealing's effect on Sample 4, and Table 2.1 shows the final Fermi level of the annealed samples. There was some

variability in the annealing results, similar to those seen by Walsh [15]. Note that a 220 °C anneal on Sample 1 did not have the desired effect and actually lowered the Fermi level. This observation shows that there is some variability in the process, but overall, a general trend was observed where the Fermi level increased with respect to annealing temperature and time.

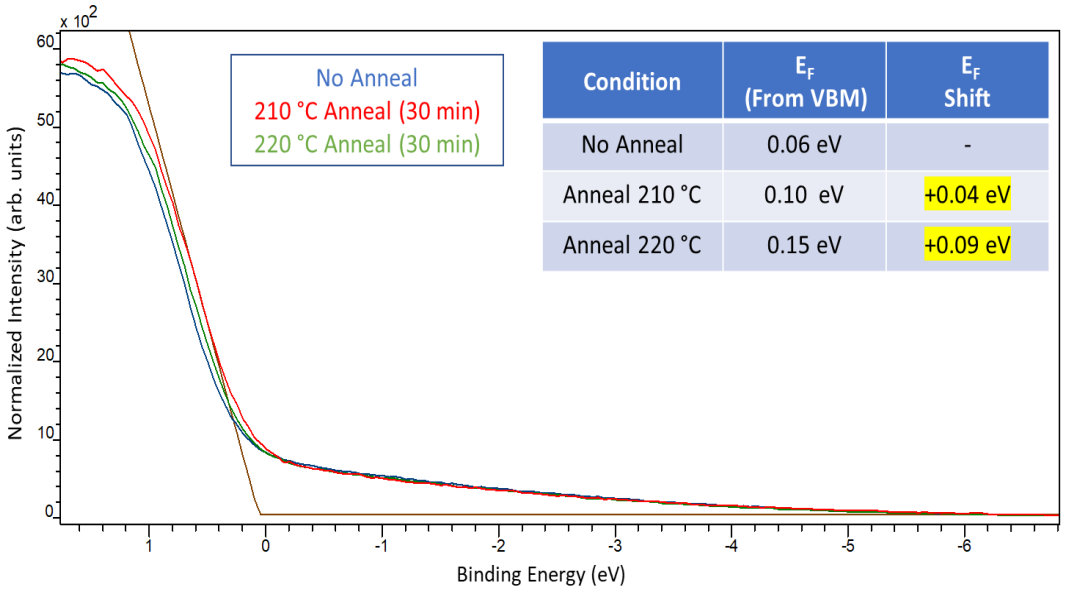

Figure 2.6 - XPS Measurements showing the effect of annealing Bi_2Se_3 in UHV on the valence band edge. Fermi level shifted by 0.04 eV for 210 °C anneal, and 0.09 eV for 220 °C anneal.

TABLE 2.1

XPS MEASUREMENT OF FERMI LEVELS FOR EACH BI_2SE_3 FILMS AFTER ANNEALING IN UHV

Layer	E_F - Sample 1	E_F - Sample 2	E_F - Sample 3	E_F - Sample 4
As-grown Film	0.08 eV	0.06 eV	0.06 eV	0.06 eV
Annealed Film	(220 ° anneal for 30 min) 0.06 eV	(220 ° anneal for 30 min) 0.13 eV	(220 ° anneal for 30 min) 0.09 eV	(210 ° anneal for 30 min + 220 ° anneal for 30 min) 0.15 eV

NOTE: Fermi Level is with reference to the Valence Band Edge

The WSe_2 deposition, even though it was done under Se flux, was observed to affect the previously measured Fermi levels. For that reason, an analysis on the core level electrons was done after the WSe_2 growth as well. This analysis is shown in the WSe_2 section below and the observed effect was enough to rethink the duration of the UHV anneal. For that reason, Sample 4 was annealed longer compared to samples 1, 2 and 3 which were grown later since the post-WSe_2 deposition Fermi levels was getting too close to the conduction band.

2.3 Growth of Tungsten Diselenide

To explore the effects of WSe_2 film thickness on the transport behavior of the diode, four samples were grown with different growth times.

- Sample 1 was grown for 3 hours

- Sample 2 was grown for 5 hours
- Sample 3 was grown for 7 hours
- Sample 4 was grown for 9 hours

2.3.1 WSe_2 on Bi_2Se_3 Interface

As discussed before, van der Waals epitaxy has the added benefit of reducing the requirement for lattice matching due to the diminished strain between van der Waal interfaces. Previous work by Yue *et al.* [20] show that even though there is a 21% lattice mismatch between Bi_2Se_3 and WSe_2, the van der Waal bonds allowed for relaxed growth with no misfit dislocations. Figure 2.6 shows a TEM measurement of Yue's Bi_2Se_3 on WSe_2 which shows the high quality growth attainable for these type of 2D interfaces.

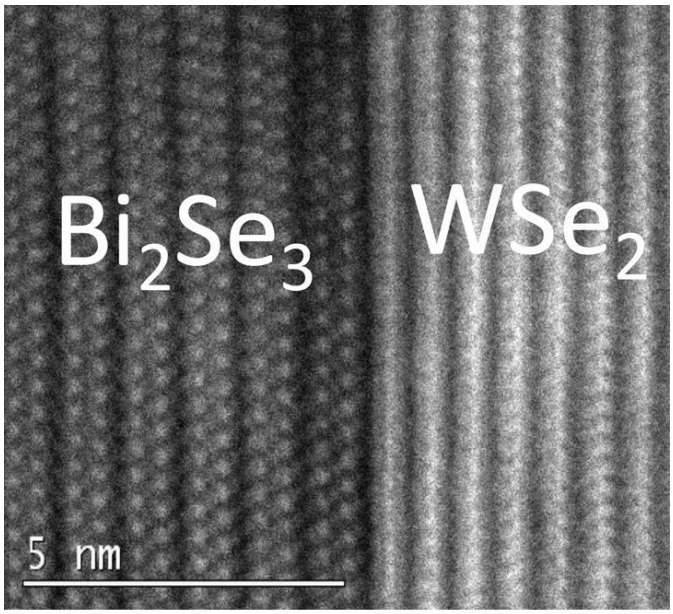

Figure 2.7 - TEM image of Bi_2Se_3 Growth on WSe_2 showing the abrupt interface with no signs of mislocations. Reprinted with permission from [20] © 2017 IOP Publishing Ltd.

2.3.2 Tungsten Diselenide Growth Parameters

WSe_2 films were grown on top of the Bi_2Se_3 as the tunnel barrier for the device. During growth, the bismuth k-cell was kept at 490 °C producing a flux of 3 x 10^{-9} mbar as measured by Beam Flux Monitor (BFM) while the Se TCC was kept at 200 °C for its reservoir and 1000 °C for its cracker for a flux of 2.3 x 10^{-5} mbar. The substrate temperature used was 280 °C. As the substrate ramped up to this temperature, the Se shutter was opened for temperatures above 160 °C until the desired growth temperature was achieved.

RHEED was used to evaluate the integration and growth of the WSe_2 onto the Bi_2Se_3 structure. Figure 2.8 shows the RHEED pattern in the sample as the WSe_2 was grown on top of the Bi_2Se_3. The WSe_2 diffraction pattern coexists with the Bi_2Se_3 pattern as the first monolayer gets grown. This indicates that there is no amorphous buffer layer in between Bi_2Se_3 and WSe_2, but instead, there is a sharp transition between the two. Moreover, the azimuthal alignment of the RHEED pattern observed confirms rotational alignment to the surface of the Bi_2Se_3. The time to full coverage of the WSe_2 film differed from each growth, varying between ~2 hours for Sample 1 and Sample 3, and ~1.5 hours for Sample 2 and Sample 4.

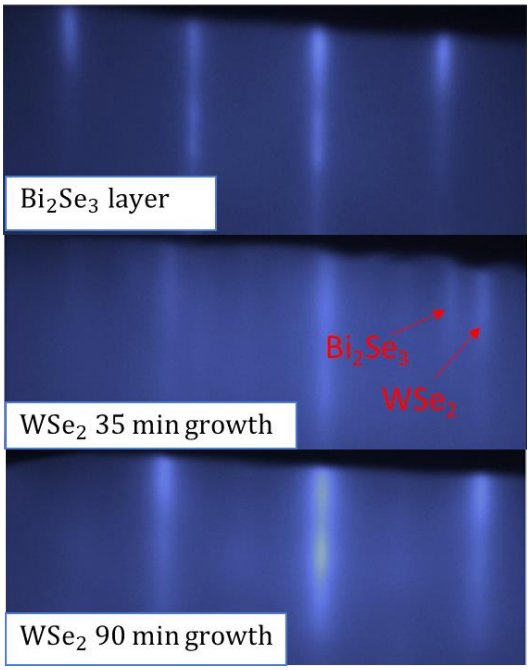

Figure 2.8 - RHEED pattern during WSe_2 growth. Both RHEED patterns for Bi_2Se_3 and WSe_2 coexist at the same time before WSe_2 fully covers the Bi_2Se_3.

2.3.3 Thickness Measurement

XPS was used to find the thickness of the WSe_2 layer based on the intensity ratio between photoemission peaks recorded for the WSe_2 layer and the Bi_2Se_3 film underneath. As the thickness of the WSe_2 increases, the signal from the Bi_2Se_3 films gets attenuated. This attenuation in peak intensity can be used to obtain an estimated thickness of the WSe_2 overlayer based on the atomic density of the substrate and the overlayer.

The XPS measurements used for these calculations were made at 0˚ and 45˚. The additional 45° measurement was obtained to increase the surface sensitivity of XPS. The penetration depth of the x-ray decreases by $\cos(\theta)$, where θ is the angle of inclination to the normal of the surface (As seen in Figure 2.9). A reduction of 30% to the penetration depth was expected for an angle of 45˚.

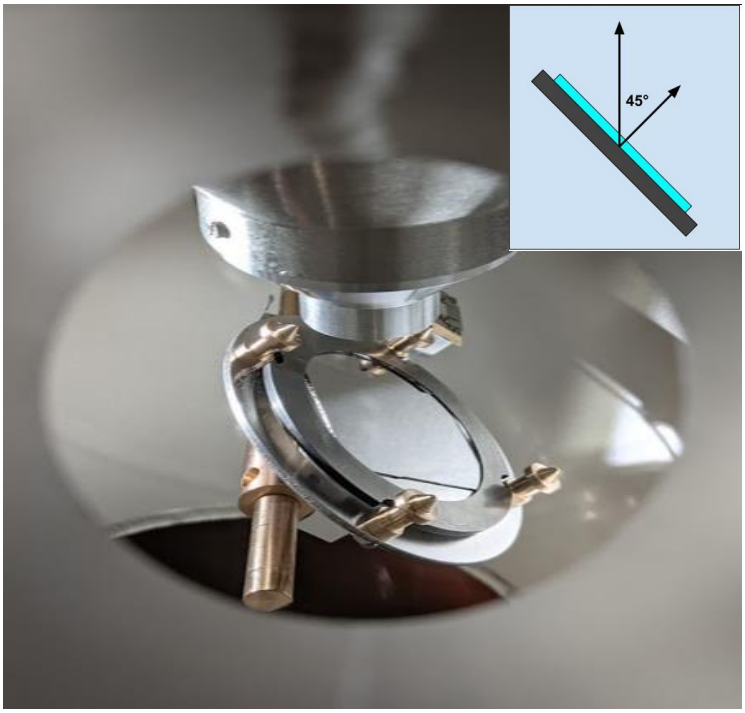

Figure 2.9 - Showing the setup for the XPS measurement of the sample at a 45° angle

The peak intensity is defined as the area under the photoemission peak while discounting the electron background. The peak intensities were calculated using CasaXPS while applying a Shirley electron background. W $4f_{7/2}$ and Bi $4d_{5/2}$ (seen in Figure 2.10 (A)) were utilized for the photoemission calculation as the photoemission peaks of the overlayer and the substrate, respectively. First, the photoemission peaks are close enough to each other to ignore the transmission function's contributions and other effects that far away peaks would need correction for more accurate measurements. Second, the W peaks with lower kinetic energies require more sampling time due to the noise from the electron background made by higher kinetic energy electrons. Third, the Bi peaks that did not require substantially more probing due to having the second

problem were convoluted with Se and W peaks and added a degree of ambiguity to the measurement.

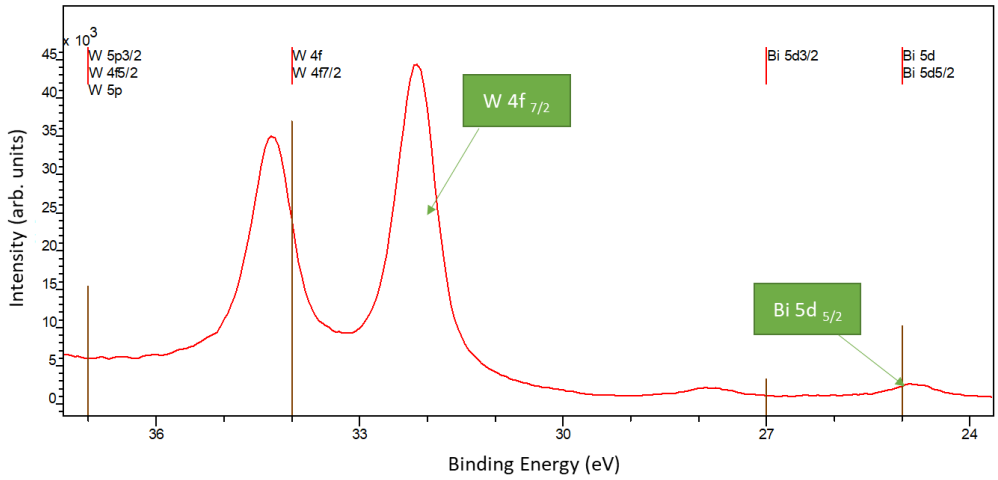

A

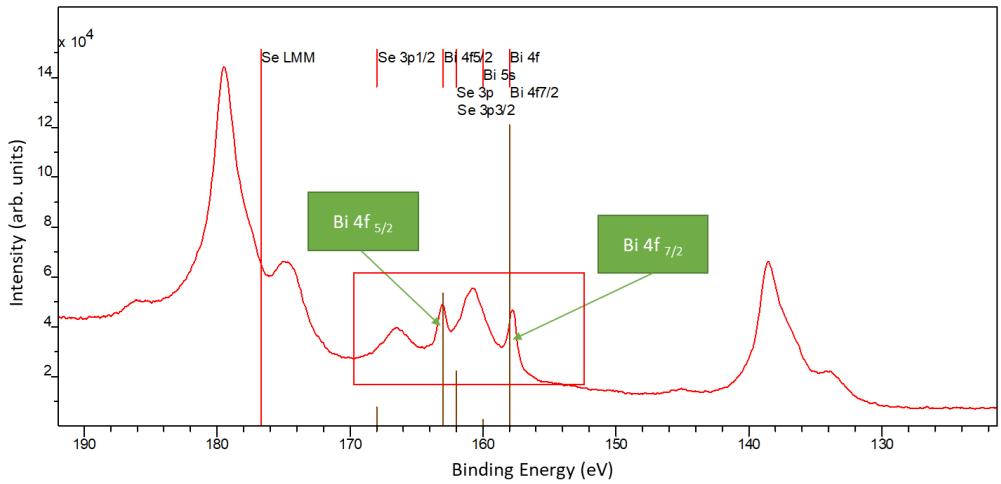

B

Figure 2.10 - XPS Spectrum of potential photoemission peaks for thickness measurement comparison. The peak intensity is the area under each photoemission peak. (A) Photoemission peaks W 4f $_{7/2}$ and Bi 4f$_{5/2}$ used to determine thickness. Peaks show little convolution, with closed proximity. (B) Bi 4f$_{5/2}$ and Bi 4f$_{7/2,}$ which are the largest Bi peaks have no W peaks around and are convoluted with Se peaks.

For the thickness measurement of WSe_2, an overlayer model was used, and calculations were performed in nanohub using "XPS Thickness Solver" [21] since it provided the highest accuracy compared to other models encountered [21]–[23]. Zemlyanov showed measurements that were consistent with TEM measurement with monolayer precision in films with uniformity, while having a slight overestimation in non-uniform films [22]. The tool is perfect for quick characterization of the WSe_2 without doing any ex-situ measurements like TEM.

To solve for the thickness, the atomic densities were required and were calculated from the unit cell of each material. The atomic density of Bi and W in the substrate and overlayer were found to be 1.29×10^{22} atoms/cm^3 and 1.38×10^{22} atoms/cm^3. The relative sensitivity factor for Bi $4d_{5/2}$ is 1.76 and for W $4f_{7/2}$ is 5.48 according to the CasaXPS library. The asymmetry parameters were obtained from a database by Band et al [24] and were 1.05 for W and 1.15 for Bi. The inelastic mean free paths were obtained from the NIST Electron Effective-Attenuation-Length Database V 1.3 [25], which utilized the TPP-2M predictive formula. The following IMFPs were obtained:

- Overlayer photoelectrons (W $4f_{7/2}$) through overlayer: 2.61 nm
- Substrate photoelectrons (Bi $4d_{5/2}$) through overlayer: 2.62 nm
- Substrate photoelectrons (Bi $4d_{5/2}$) through substrate: 2.90 nm

The results of the thickness calculations are described in Table 2.2 based on the 0° and 45° measurements. The thickness from Sample 1 and Sample 2 agree with the observed full coverage of the WSe_2 RHEED pattern on the Bi_2Se_3 pattern. Observation of full coverage of the 2-D materials like WSe_2 has been a reliable form of film thickness measurements for WSe_2.

TABLE 2.2

ESTIMATED THICKNESS AND GROWTH RATE OF WSE2 LAYER FOR EPITAXIALLY GROWN SAMPLES

Layer	**Sample 1 (3 Hr. Growth)**	**Sample 2 (5 Hr. Growth)**	**Sample 3 (7 Hour Growth)**	**Sample 4 (9 Hour Growth)**
0° measurement	1.2 nm (1.7 monolayers)	3.0 nm (4.2 monolayers)	3.3 nm (4.7 monolayers)	5.4 nm (7.7 monolayers)
Growth Rate	0.6 monolayers/hr	0.9 monolayers/hr	0.7 monolayers/hr	0.9 monolayers/hr
45° measurement	1.1 nm (1.7 monolayers)	2.8 nm (4.0 monolayers)	4.1 nm (5.8 monolayers)	7.8 nm (11.1 monolayers)
Growth Rate	0.6 monolayers/hr	0.8 monolayers/hr	0.8 monolayers/hr	1.2 monolayers/hr

Sample 1 and Sample 2 had the most consistent measurements between the four samples. This might indicate that larger growth times increase the non-uniformity of the WSe_2 film since as the substrate is inclined for the 45° measurement, the incident X-ray area increases and covers more area.

In terms of tunneling, since tunnel barrier thicknesses are usually of the order of 3 nm or less, Sample 3 and Sample 4 may have difficulty in observing the tunneling since they likely have too low of a tunneling probability due to overly thick barriers.

2.3.4 Unintentional Selenium Vacancies on Bi_2Se_3

Now that the WSe_2 growth has been discussed, one can revisit the problem from Section 2.2.3. The WSe_2 growth on top of the Bi_2Se_3 was done at 280 °C, a temperature 60 °C higher than the Bi_2Se_3 growth temperature and the previously done anneal steps. Unlike the UHV anneal step for Fermi level tuning however, the growths at those temperatures were done under Se pressure, but this is not a guarantee for annealing to no induce new dopants (Se vacancies). Resolving the position of the post-deposition Fermi level required an analysis of the core level electrons of Bi_2Se_3. Since every electron energy level has the Fermi level as a reference point, it is assumed that shifts in the Fermi level of the Bi_2Se_3 sample will correlate with shifts in the measured core level electrons of Bi_2Se_3. Moreover, since the thickness of the WSe_2 was less than the escape depth of the photoelectrons (as seen in Section 2.3.3), XPS could be used to probe the core level electrons from the Bi_2Se_3 underneath.

Bi $4f_{7/2}$ was shown by Walsh to move closely with respect to changes in the Fermi level, and served as a good estimate of any further changes to the Fermi level and was used as a reference point [15]. Like Walsh, the XPS measurements showed a similar correlation of results with the Bi 4f electrons when UHV anneals were done. Figure 2.11 shows the aforementioned shifts in the Bi $4f_{7/2}$ and Bi $5d_{5/2}$ peaks before and after annealing, and also the shift of these core level electrons after the WSe_2 deposition.

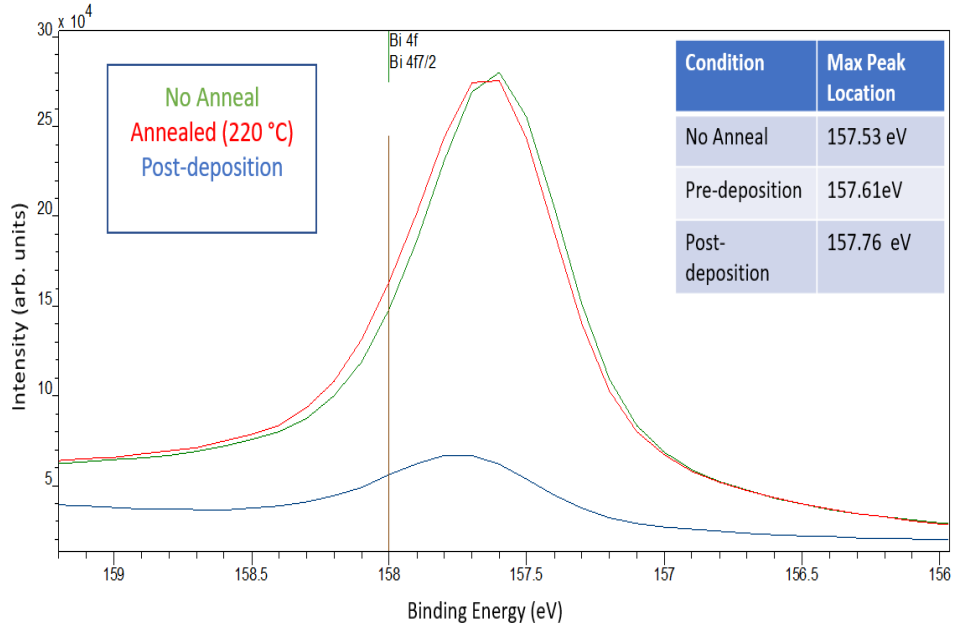

A

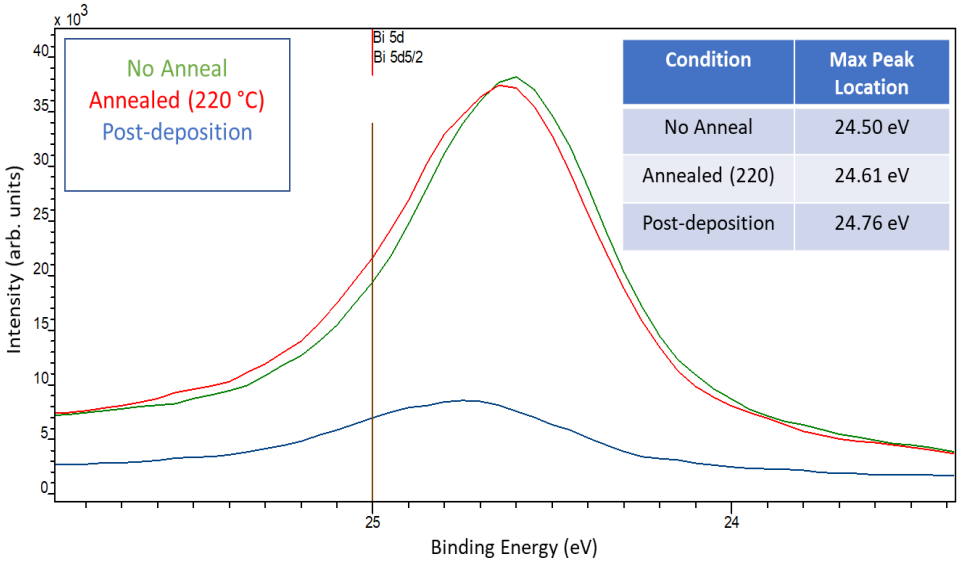

B

Figure 2.11 - XPS measurement of (A) Bi $4f_{7/2}$ and (B) Bi $5d_{5/2}$ for Sample 4. Fermi level shift after UHV anneal at 220 °C is 0.09 eV, close to the observed 0.08 eV shift on the Bi $4f_{7/2}$ peaks.

The final Fermi level was estimated after adding the energy shift of Bi $4f_{7/2}$ to the previously obtained Fermi level. After the WSe_2 growth, the last Bi_2Se_3 layer was grown for 60 minutes, and the VBM edge was obtained after that. Table 2.2.3 shows the estimated Fermi levels with respect to the valence band for the top and bottom film. Sample 4 is the closest to the conduction band.

TABLE 2.3

XPS MEASUREMENT OF FERMI LEVELS FOR EACH BI_2SE_3 FILMS AFTER WSE_2 DEPOSITION

Layer	**E_F - Sample 1**	**E_F - Sample 2**	**E_F - Sample 3**	**E_F - Sample 4**
Bottom Film	0.2324 eV	0.2447 eV	0.2015 eV	0.2985 eV
Top Film	0.0795 eV	0.0602 eV	0.0612 eV	0.0915 eV

NOTE: Fermi level is with respect to valence band edge.

Any further changes that happened after the WSe_2 were not accounted since the top Bi_2Se_3 layer was thicker than the photoelectron escape depth. The Bi_2Se_3 growth was done under Se flux and at the same growth temperature as the bottom Bi_2Se_3 making it unlikely that the Fermi level of the bottom Bi_2Se_3 changes much more.

CHAPTER 3:

DEVICE FABRICATION AND CHARACTERIZATION

3.1 Device Fabrication

The heterostructure synthesized by MBE was used to fabricate devices. The goal of the design was to minimize the amount of damage on the Bi_2Se_3 layers due to fabrication that could cause further selenium vacancies.

Initially, the first samples were fabricated from heterostructures grown on sapphire (not the same samples as those characterized above), where a silicon wafer was used as a hard mask to create a step in the heterostructure. This was an attempt to avoid etching induced damage. The films still had to be etched to isolate the devices from each other and two metal contacts had to be deposited on each side of the step, but the damage to the film was considerably reduced by using this hard mask. The silicon hard mask growths on sapphire were unsuccessful due to capillary growth under the silicon hard mask resulting in a short between the top and bottom Bi_2Se_3 layers.

After that attempt, a new process flow was devised that utilized an additional etch followed by the metallization for the contacts. The etching was challenging to reproduce as the WSe_2 layer was considerably more robust to the Cl_2 etch than Bi_2Se_3, resulting in a non-uniform, rough Bi_2Se_3.

At this point, the option of having a conductive substrate was considered using Bansal's recipe. A test growth with an n-type highly arsenic doped Si (111) was

performed. The growth did not suffer from any noticeable deterioration compared to Bansal's and had a repeatable RHEED pattern.

A mesa etch fabrication was utilized as the final design for the device which used the Si (111) substrate as the bottom contact to the Bi_2Se_3. The final design is shown in Figure 3.3. The Si substrates have a resistivity of 0.004 - 0.005 Ω/cm as measured by FPP5000 Four Point Probe and correspond to a doping concentration of approximately 1×10^{19} cm^{-3}.

The final fabrication process involved four steps for the mesa etch of the heterostructure using a top contact (Au e-beam evaporation, photolithography, wet etch, and dry etch) and one step for the bottom contact (Ti/Al sputter). Figure 3.1 shows the starting point of the fabrication, while Figure 3.2 and Figure 3.3 show the full fabrication process.

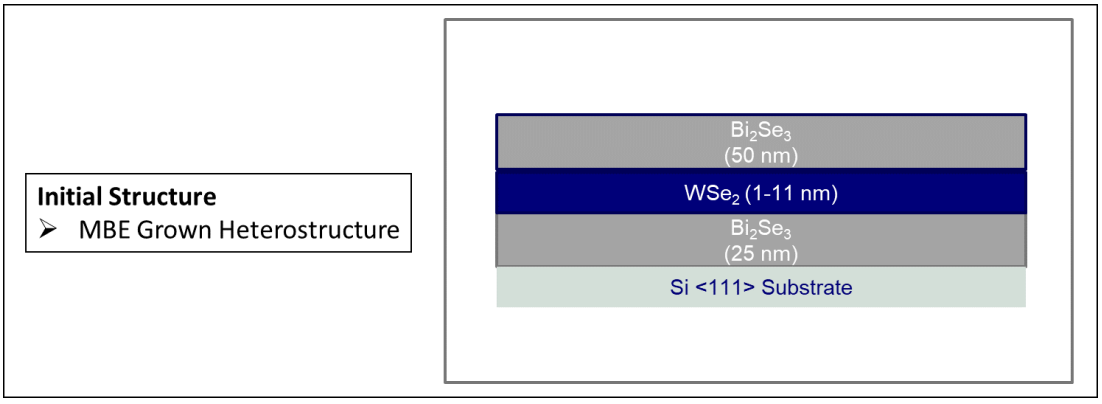

Figure 3.1 - Initial structure before fabrication.

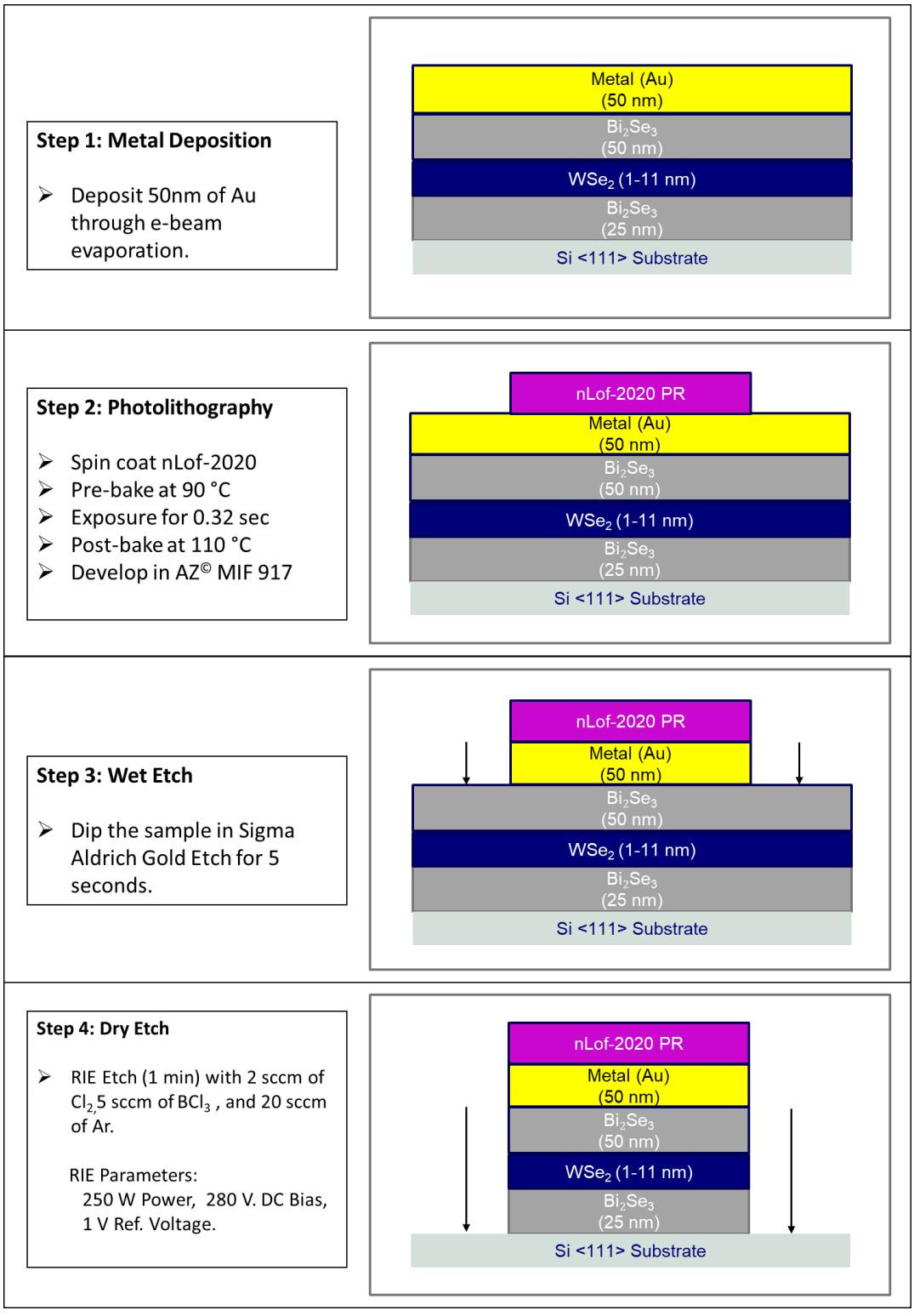

Figure 3.2 - Final fabrication steps for the patterning of heterostructure and top contact.

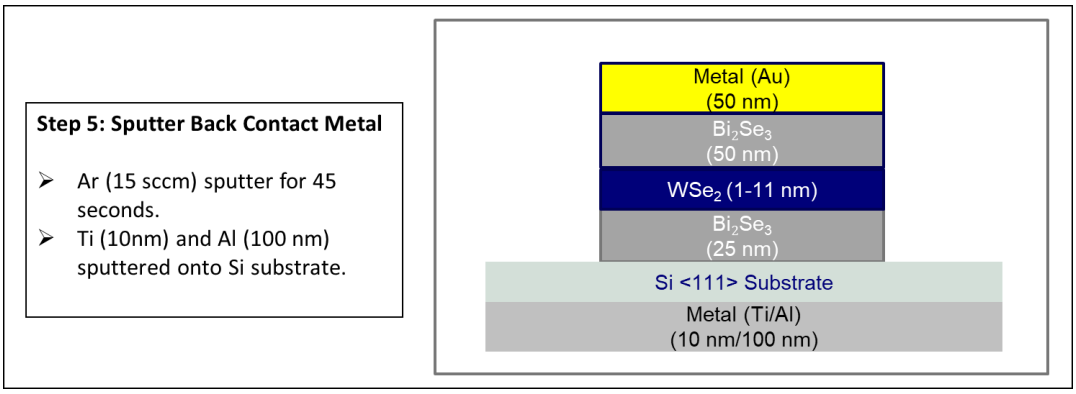

Figure 3.3 - Final bottom contact sputtering step.

3.1.1 Fabrication (Top Contact and Mesa Structure)

Fabrication starts with the application of a metal contact to the heterostructure as can be seen in Figure 3.2. Lift-off is more difficult with van der Waal materials due to the lack of covalent bonds, therefore the gold was evaporated on top of the material and then etched. Gold was evaporated using a FC-1800 Electron Beam Vacuum Deposition system by AIRCO. Gold is known to exhibit reactivity yet ohmic behavior on Bi_2Se_3, and since the primary goal is to cause minimal damage to the Bi_2Se_3 possible, it was the best choice for a metal contact. However, while gold has low reactivity with Bi_2Se_3, it is not entirely non-reactive. After a specific thickness, multiple reports have described that Bi_2Se_3 starts to react with gold [26], [27], [27], [28]. Therefore, a thickness of no more than 50 nm of gold was used as a top contact. At around 100-150 nm of gold deposition, the Bi_2Se_3 turned black after the gold was etched and, its resistivity was considerably higher than the resistivity of pre-deposited Bi_2Se_3.

The photolithography process was done by first applying the gold-coated sample with HMDS to enhance the photoresist's adhesion, after which negative photoresist nLof-2020 was applied by spin-coating at 4000 RPM for 1 min and pre-baked to 90 °C for

another minute. The photolithographic exposure was done in a GCA AutoStep 200 i-Line Wafer Stepper with an exposure of 0.32 sec. The sample was then post-baked at 110 °C and developed in AZ 917 MIF Developer for 30 sec.

The photoresist mask was used to pattern the gold layer with a wet etch using Sigma Aldrich's Gold Etch. The wet etch was 5 seconds long. The reason behind the wet etch was that gold and other noble metals like Pd, Ag, and Pt are challenging to dry etch without heavily depositing on the sides of the sample as the initial Bi_2Se_3 samples attested. Previously, an aqua regia bath was used to etch the gold pattern, but the Bi_2Se_3 resistivity was considerably lowered afterward.

Moreover, Aqua Regia and dry etches with a higher percentage of Cl_2 resulted in the heterostructure having stronger adhesion to the substrate and having an insulating residue on top of the film, as can be seen in Figure 3.4. These heterostructures would not scratch off as easily as standard 2D materials and were also able to survive a 10-second ultrasonic bath (a feat almost impossible for average van der Waal materials as they would peel off even at the lowest settings). This might suggest that some of the bottom Bi_2Se_3 has covalent bonding with the 3D Si substrate.

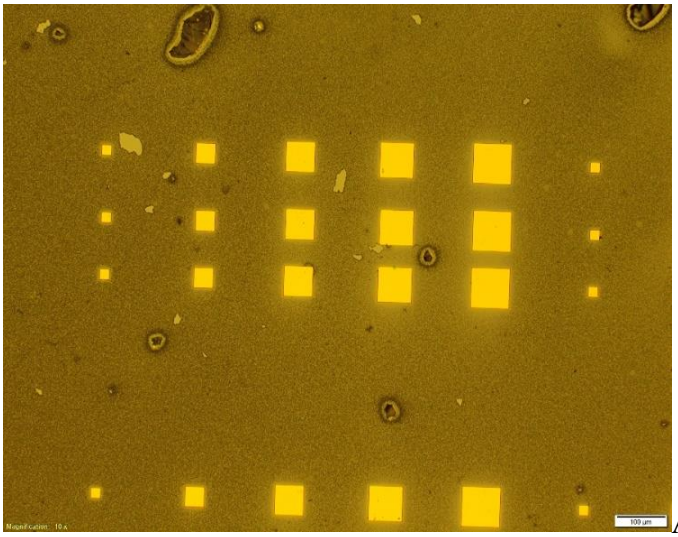
A

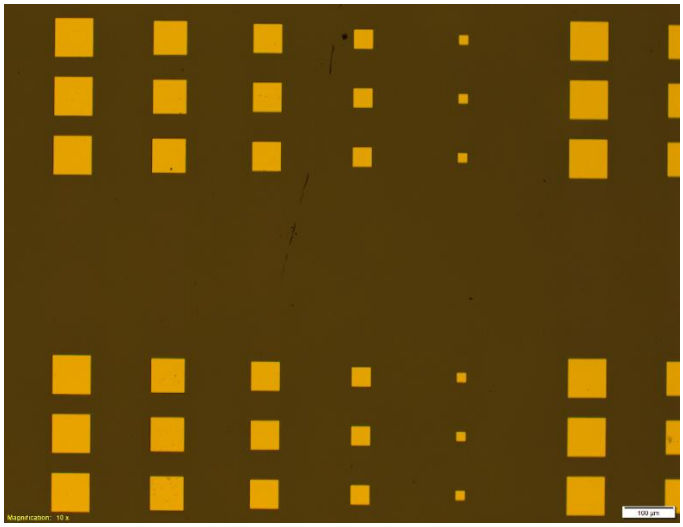
B

Figure 3.4 - (A) Surface after 10 sccm of Cl_2 and 5 sccm of Ar with 150 W of power applied and 50 V Forward Bias for 1 min. Residue is scratchable, but would not dry etch any further. (B) Film etched with the new recipe with higher Ar concentration.

After the wet etch, a $Cl_2/BCl_3/Ar$ (2 sccm/5 sccm/20 sccm) dry etch was used to finish etching down to the substrate. The dry etch was done at 250 W power with 280 V DC Bias. The dry etch time needed depended on the sample, but 1 min and 10 seconds was enough to completely etch through down to the substrate.

Once the etching step finished, the nLof-2020 was lifted using an 80 °C two-bath PG remover process for 10 min with an extra dip in IPA and a final rinse in DI water. Any attempts to use acetone to strip or oxygen plasma to ash the photoresist ended up in a hardened photoresist film that could not be removed.

3.1.2 Fabrication (Bottom Contact)

The bottom contact's fabrication was easier since there was only the need to deposit an ohmic metal contact on the backside after sputtering the silicon. This step is to remove any native oxide that exists on the back of the sample and ensure proper contact with the probes. The sample's back was scratched with a diamond scribe as an extra cautionary step to remove the oxide. The sample was then loaded into the Oerlikon 450B Sputtering system's load lock and sputtered with Ar to ensure the native oxide was removed. 10 nm of titanium and 100 nm of aluminum were sputtered on the back of the sample as a back contact.

3.2 Results

Figure 3.5 shows an example I-V curve measured at -50 °C. The devices tested did not obtain the desired negative differential resistance in any of their I-V curves at the current temperature of -50 °C. However, results were analyzed to tune the device even further in future experiments. Also, an explanation of how the electrical characterization and lookout for NDR was done is explained below.

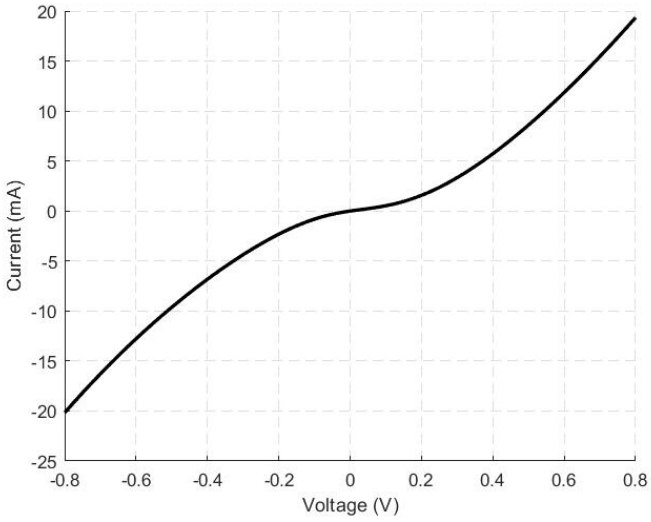

Figure 3.5 - Sample 1 (1.2 nm WSe_2 thickness) I-V Curve at -50 °C. No NDR was observed at -50 °C temperatures on any of the samples.

To begin, one must remember some facts about Bi_2Se_3. Bi_2Se_3's Dirac cone lies inside a 0.3 eV bandgap. At this small bandgap, thermal effects become important and low temperature is needed in attempts to observe the tunneling phenomena. At 300 K, the thermal energy allows for bulk conduction through the conduction band. To minimize this effect, the samples had to be cooled down. I-V Measurements were made in a B1500A Device Analyzer from Agilent Technologies and included Temptronix Thermochuck. Moreover, for the purpose of temperature-dependent I-V measurements, the samples were measured at five different temperatures: -50 °C, -25 °C, -0 °C, 25 °C, and 75 °C. The temperature-dependent I-V curves were performed in two directions: one from 25 °C down to -50 °C and the other one from -50 °C up to 75 °C.

3.2.1 I-V Measurement

Figure 3.6 shows the current density for Sample 1 through Sample 4 at room temperature. The thickness of the WSe_2 does not seem to follow a trend where decreasing

thickness implies more current, which was surprising. Sample 4, which had the highest current density, also had the thickest film. There are multiple reasons for this which are explored in this section.

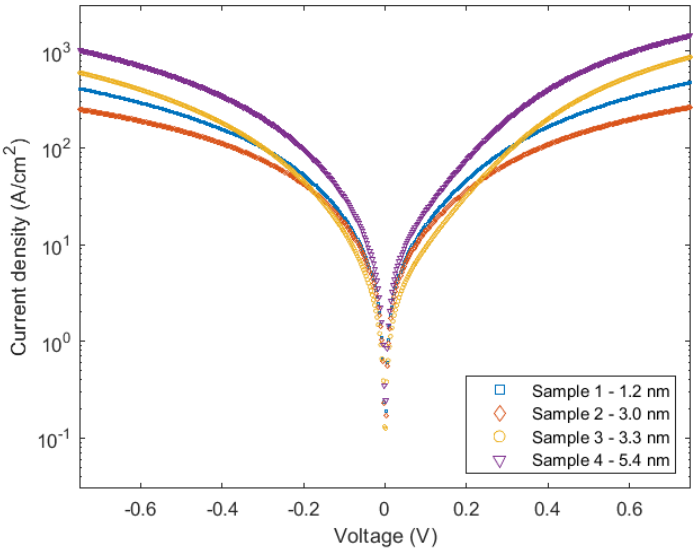

Figure 3.6 - Current density of all samples at room temperature (upsweep measurement).

Ignoring the anomaly of Sample 3, which will be explained later, Figure 3.7 shows a temperature-dependent process dominating the I-V curves between 75 °C and 0 °C and diverging around -25 °C. The temperature dependence indicates thermionic emission rather than tunneling emission at room temperature, which may explain part of the negative correlation between the samples' currents and their barrier thicknesses in Figure 3.6 at higher voltages.

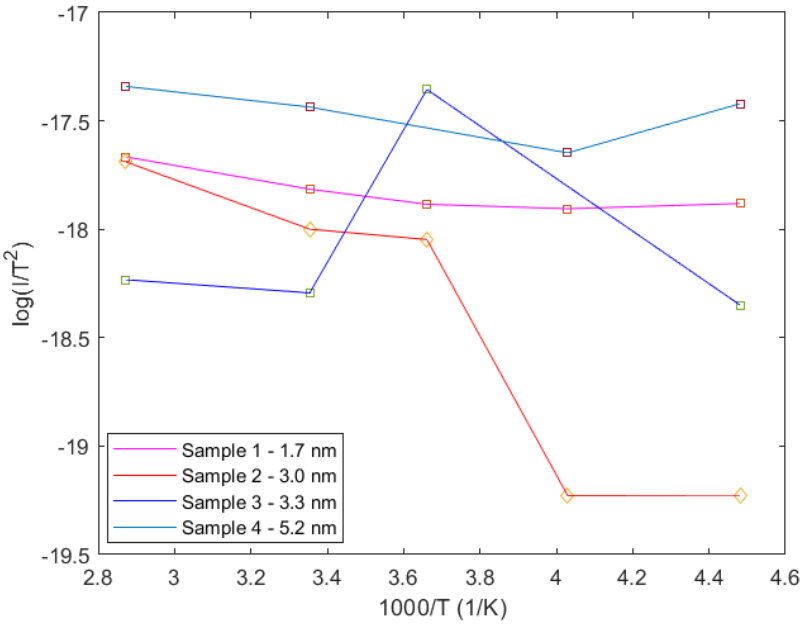

Figure 3.7 – Richardson plot showing temperature dependence of Sample 1 through Sample 4. Measurement was made at 0.14 V.

Assuming a current density undergoing thermionic emission modeled after a MIM structure [29]:

$$J = A * T^{2} * \exp\left(-\frac{\varphi}{k_B T}\right) * \left(1 - \exp\left(-e * \frac{V}{k_B T}\right)\right) \qquad (3.1)$$

Where A is the Richardson's constant, T is temperature, k_B is the Boltzmann constant, e is the electron charge, V is the applied voltage, and φ is the barrier height. In this context, the current is independent of the thickness of the barrier. Contrasted to an oxide layer where the thickness matters since thermionic emissions are negligible at such large band gaps (8.4-11 eV), the WSe_2 does not have a large bandgap (1.2-1.6 eV). Moreover, WSe_2 as a monolayer and bilayer has a larger bandgap (1.4-1.6 eV) than bulk WSe_2 (1.2 eV). This might explain the smaller current density observed in Sample 1 compared to Sample 4 as it had a thickness of 1-2 monolayers compared to the other

samples with four or more monolayers. Given that Sample 1 is in the right thickness to observe tunneling behavior, the sharp increase in current between 0.0 V and 0.2 V might be due to tunneling. After that, thermionic emission starts to dominate, and Sample 1 is scaled in Eq 3.1 with a different exp $(-\frac{\varphi}{k_B T})$ constant than the others given the larger bandgap.

Figure 3.8-3.12 (A),(B) shows the multi-temperature results measured in the Agilent device analyzer, and Figure 3.8 – 3.12 (C) shows the Richardson plot of the upsweep. Sample 1 was the most well-behaved between its I-V curve's upsweep and downsweep, while Sample 3 and Sample 4 show variation in their I-V curves between sweeps compared to Sample 1. The variation in Sample 3's I-V curves causes the sharp anomaly in the Richardson plot of Sample 3 seen in Figure 3.10 (C) as the 0 °C measurement is larger than the rest at 0.14 V. The variations in the I-V curves between the downsweep and the upsweep indicate the presence of traps in the tunnel barrier. These traps allow for trap-induced tunneling to happen. Moreover, looking back into the discrepancy in the XPS measurement results at 0 ° and 45 ° for Sample 3 and Sample 4, this variation also aligns with a non-uniformity of the WSe_2 film. In that case, the thickness of the barrier measured by XPS might have thinner or thicker sections in the film than it is believed as the measurement averages the number of layers [22].

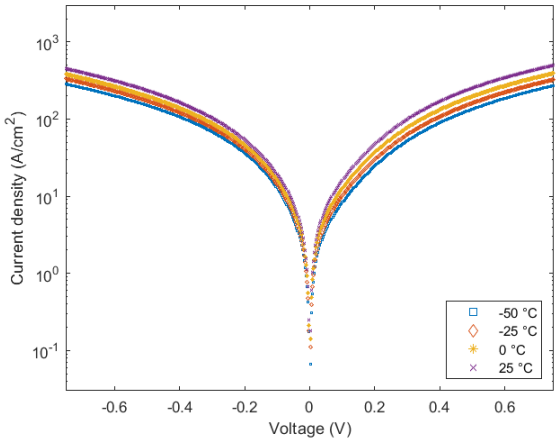

A

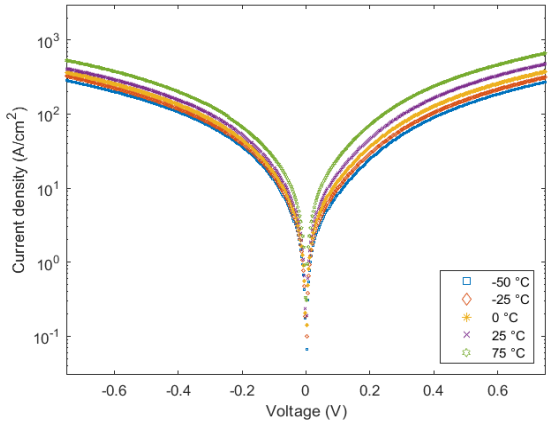

B

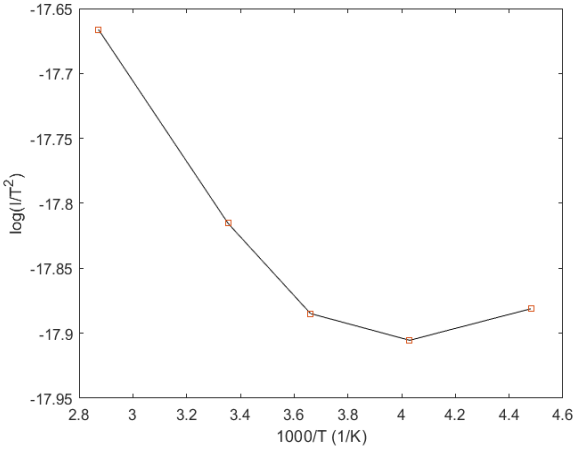

C

Figure 3.8 - Temperature-dependent I-V Measurement of Sample 1 (1.7 nm WSe_2 thickness). (A) Temperature Sweep from 25 °C to -50 °C. (B) Temperature Sweep from -50 °C to 75 °C. (C) Richardson plot of second sweep from -50 °C to 75 °C.

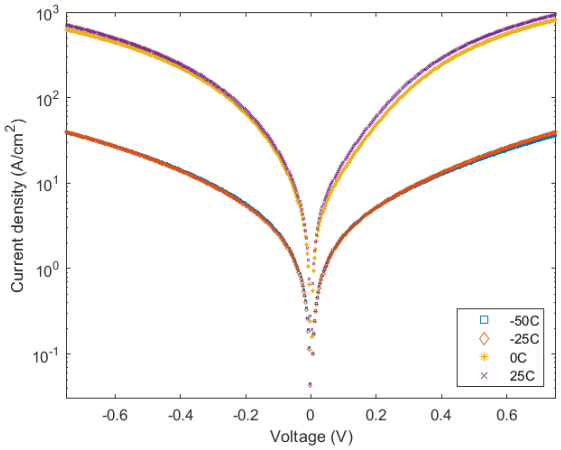

A

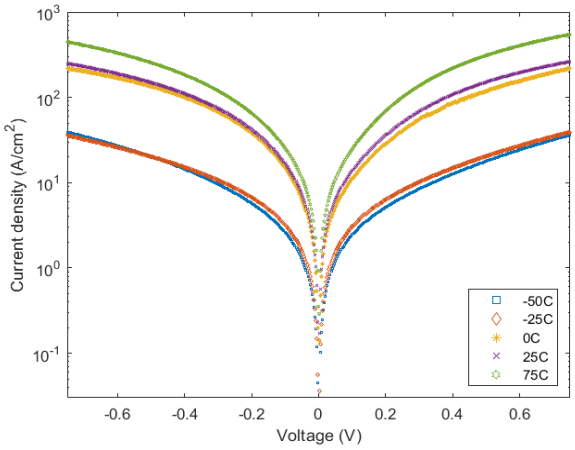

B

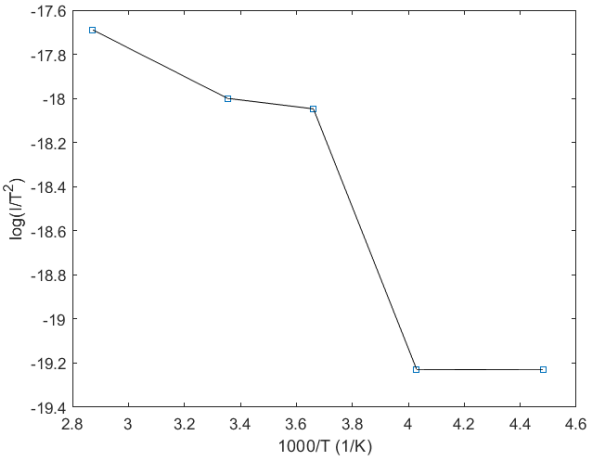

C

Figure 3.9 - Temperature-dependent I-V Measurement of Sample 2 (3.0 nm WSe_2 thickness). (A) Temperature Sweep from 25 °C to -50 °C. (B) Temperature Sweep from -50 °C to 75 °C. (C) Richardson plot of second sweep from -50 °C to 75 °C.

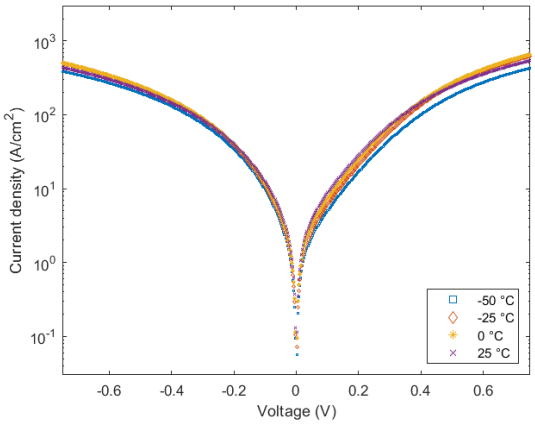

A

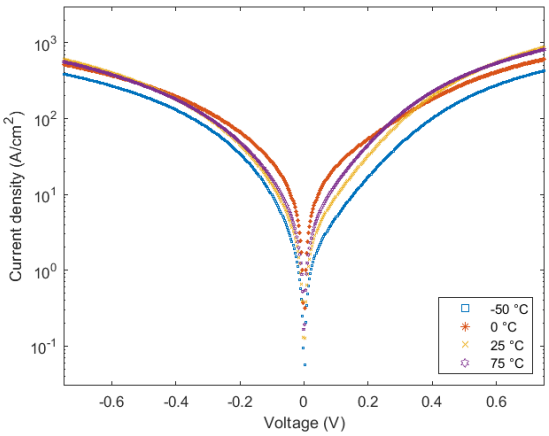

B

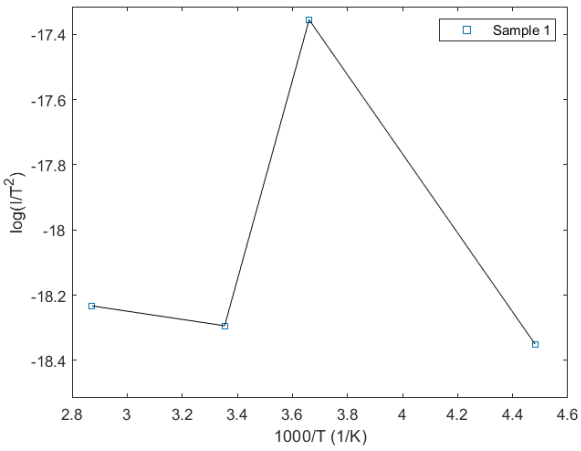

C

Figure 3.10 - Temperature-dependent I-V Measurement of Sample 3 (3.3 nm WSe_2 thickness). (A) Temperature Sweep from 25 °C to -50 °C. (B) Temperature Sweep from -50 °C to 75 °C. (C) Richardson plot of the second sweep from -50 °C to 75 °C.

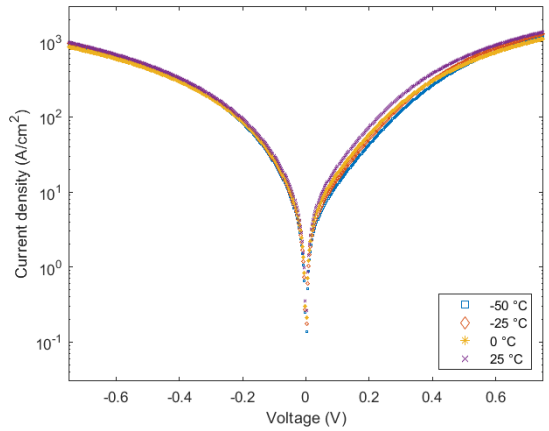

A

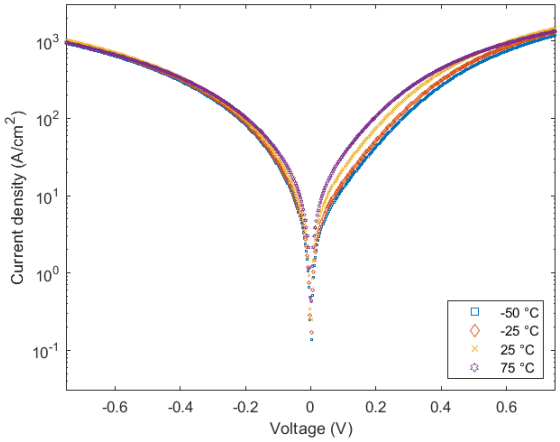

B

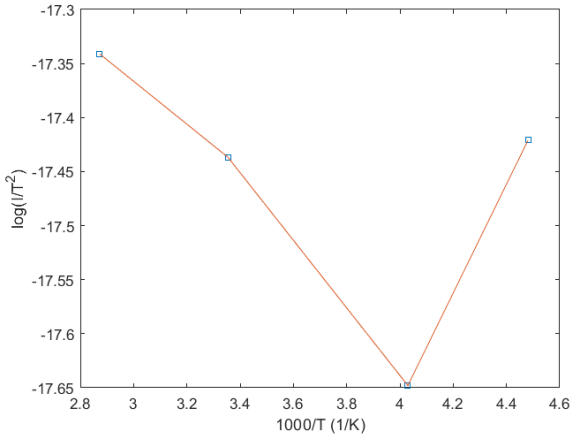

C

Figure 3.11 - Temperature-dependent I-V Measurement of Sample 4. (5.4 nm WSe_2 thickness). (A) Temperature Sweep from 25 °C to -50 °C. (B) Temperature Sweep from -50 °C to 75 °C. (C) Richardson plot of the second sweep from -50 °C to 75 °C.

The increased number of traps and thickness non-uniformity of the WSe_2 layer, the smaller bandgap, and a more pronounced bulk conduction tunneling due to the Fermi level being next to the bulk conduction band in Sample 4, causes it to have the largest current density of all the samples. Samples 1, 2, and 3 follow, as shown in the Richardson plot of Figure 3.7, which agrees with the thickness dependence at 0.14 V.

Sample 2 is interesting because there is a noticeable gap in the current density between -25 °C and 0 °C. As Sample 2 has an appropriate thickness for a tunnel barrier of 3.0 nm, this sample may be structured with the best chance of observing the spin-filtered tunneling, but further testing and analysis is required.

CHAPTER 4:

CONCLUSIONS AND FURTHER WORK

Considerable progress has been made in the heterostructure growth and characterization while attaining reproducible crystal growth results for the Bi_2Se_3. Fermi level tuning has proven reliable in moving the Fermi level to a more favorable location, and XPS thickness measurements agree with the growth rates observed by RHEED, providing quick in-situ tools for controlling the Fermi level of the Bi_2Se_3 layers and measuring the thickness of the tunnel barrier. Analysis and calibration of XPS results with STM like those done by Walsh [15] and TEM measurements like those done by Zemlyanov [22] will further confirm the reliability of these tools in the required settings.

Most of the uncertainty of the device's parameters comes after the molecular beam epitaxy growth. Fabrication methods and their effects on the heterostructure should be fully characterized, especially on the bismuth selenide layers. Currently, there are multiple sources of uncertainty in the fabrication process that may cause Bi_2Se_3 layers Fermi levels to fluctuate after the in-situ characterization was done. The application of chemicals onto the bismuth selenide for photolithography and etching needs to be reviewed under XPS and other characterization tools to ascertain their effects on the film. Etching might be the most important one as it most strongly alters the bismuth selenide. Walsh showed that even hydrogen sputtering n-type dopes the Bi_2Se_3 films due to the creation of selenium vacancies. However, he realized that Se annealing at 170 °C

returned the Fermi level to its place; therefore, it would be beneficial to research an extra annealing step after etching if the Fermi level gets altered sufficiently enough by the fabrication process.

Another thing is that uniformity of the WSe_2 may have to be analyzed further using this recipe. The I-V curves and XPS measurements show uniformity starts to change between Sample 1-2 and Sample 3-4. In that sense, future characterization using AFM might be necessary if thicknesses above 3-4 nm are desired to reduce the non-uniformity of the tunneling barrier and reduce the number of traps in the film. Tunneling might be attenuated significantly for thicknesses above 3-4 nm, so this might not be a necessary step as long there is uniformity in the film thicknesses between 1-3 nm.

The 3.0 nm thick WSe_2 tunnel barrier sample exhibits interesting (and different) I-V characteristics compared to the thinner and thicker films, suggesting that this sample may be of the correct geometry to probe the tunneling phenomena. This structure and others with similarly thick tunnel barriers should be carefully measured, including down to 6 K, to explore the transport characteristics fully. Other tunnel barriers with larger bandgaps should also be explored to reduce thermionic emission.

The use of spin-filtering to reduce the valley current in NDR devices is a novel way of introducing new low-power devices. Nevertheless, further research needs to be done on the fabrication of the materials and devices to observe the predicted phenomena.

BIBLIOGRAPHY

[1] Nam Sung Kim *et al.*, "Leakage current: Moore's law meets static power," *Computer*, vol. 36, no. 12, pp. 68–75, Dec. 2003, doi: 10.1109/MC.2003.1250885.

[2] J. Torrejon *et al.*, "Neuromorphic computing with nanoscale spintronic oscillators," *Nature*, vol. 547, no. 7664, pp. 428–431, Jul. 2017, doi: 10.1038/nature23011.

[3] H. Farkhani, M. Tohidi, S. Farkhani, J. K. Madsen, and F. Moradi, "A Low-Power High-Speed Spintronics-Based Neuromorphic Computing System Using Real-Time Tracking Method," *IEEE J. Emerg. Sel. Top. Circuits Syst.*, vol. 8, no. 3, pp. 627–638, Sep. 2018, doi: 10.1109/JETCAS.2018.2813389.

[4] D. Silver *et al.*, "Mastering the game of Go with deep neural networks and tree search," *Nature*, vol. 529, no. 7587, pp. 484–489, Jan. 2016, doi: 10.1038/nature16961.

[5] A. M. Kurakin *et al.*, "Capacitance characterization of AlN/GaN double-barrier resonant tunnelling diodes," *Phys. Status Solidi C*, vol. 3, no. 6, pp. 2265–2269, 2006, doi: https://doi.org/10.1002/pssc.200565156.

[6] J. Falson *et al.*, "MgZnO/ZnO heterostructures with electron mobility exceeding 1×10^6 cm^2/Vs," *Sci. Rep.*, vol. 6, no. 1, p. 26598, Jul. 2016, doi: 10.1038/srep26598.

[7] T. Saku, Y. H. Y. Hirayama, and Y. H. Y. Horikoshi, "High Electron Mobility in AlGaAs/GaAs Modulation-Doped Structures," *Jpn. J. Appl. Phys.*, vol. 30, no. 5R, p. 902, May 1991, doi: 10.1143/JJAP.30.902.

[8] J. E. Moore, "The birth of topological insulators," *Nature*, vol. 464, no. 7286, Art. no. 7286, Mar. 2010, doi: 10.1038/nature08916.

[9] M. Z. Hasan and C. L. Kane, "Colloquium: Topological insulators," *Rev. Mod. Phys.*, vol. 82, no. 4, pp. 3045–3067, Nov. 2010, doi: 10.1103/RevModPhys.82.3045.

[10] C. Jozwiak *et al.*, "Spin-polarized surface resonances accompanying topological surface state formation," *Nat. Commun.*, vol. 7, no. 1, Art. no. 1, Oct. 2016, doi: 10.1038/ncomms13143.

[11] D. Hsieh *et al.*, "Observation of Unconventional Quantum Spin Textures in Topological Insulators," *Science*, vol. 323, no. 5916, pp. 919–922, Feb. 2009, doi: 10.1126/science.1167733.

[12] Y. Zhang *et al.*, "Crossover of the three-dimensional topological insulator Bi_2Se_3 to the two-dimensional limit," *Nat. Phys.*, vol. 6, no. 8, pp. 584–588, Aug. 2010, doi: 10.1038/nphys1689.

[13] Paul, Van der Heide, "X-ray Photoelectron Spectroscopy," *Wiley-Blackwell*, p. 262.

[14] J. F. Moulder and J. Chastain, Eds., *Handbook of X-ray photoelectron spectroscopy: a reference book of standard spectra for identification and interpretation of XPS data*, Update. Eden Prairie, Minn: Perkin-Elmer Corporation, 1992.

[15] L. A. Walsh *et al.*, "Fermi Level Manipulation through Native Doping in the Topological Insulator Bi_2Se_3," *ACS Nano*, vol. 12, no. 6, pp. 6310–6318, Jun. 2018, doi: 10.1021/acsnano.8b03414.

[16] N. Bansal *et al.*, "Epitaxial growth of topological insulator Bi_2Se_3 film on Si(111) with atomically sharp interface," *Thin Solid Films*, vol. 520, no. 1, pp. 224–229, Oct. 2011, doi: 10.1016/j.tsf.2011.07.033.

[17] T. P. Ginley and S. Law, "Growth of Bi_2Se_3 topological insulator films using a selenium cracker source," *J. Vac. Sci. Technol. B*, vol. 34, no. 2, p. 02L105, Feb. 2016, doi: 10.1116/1.4941134.

[18] Z. Y. Wang, H. D. Li, X. Guo, W. K. Ho, and M. H. Xie, "Growth characteristics of topological insulator Bi_2Se_3 films on different substrates," *J. Cryst. Growth*, vol. 334, no. 1, pp. 96–102, Nov. 2011, doi: 10.1016/j.jcrysgro.2011.08.029.

[19] L. A. Wray *et al.*, "A topological insulator surface under strong Coulomb, magnetic and disorder perturbations," *Nat. Phys.*, vol. 7, no. 1, pp. 32–37, Jan. 2011, doi: 10.1038/nphys1838.

[20] R. Yue *et al.*, "Nucleation and growth of WSe_2 : enabling large grain transition metal dichalcogenides," *2D Mater.*, vol. 4, no. 4, p. 045019, Sep. 2017, doi: 10.1088/2053-1583/aa8ab5.

[21] K. C. Smith, D. Saenz, D. Y. Zemlyanov, and A. A. Voevodin, "XPS Thickness Solver," 2014, doi: https://doi.org/10.4231/D3FJ29D7X.

[22] D. Y. Zemlyanov *et al.*, "Versatile technique for assessing thickness of 2D layered materials by XPS," *Nanotechnology*, vol. 29, no. 11, p. 115705, Mar. 2018, doi: 10.1088/1361-6528/aaa6ef.

[23] P. J. Cumpson, "The Thickogram: a method for easy film thickness measurement in XPS," *Surf. Interface Anal.*, vol. 29, no. 6, pp. 403–406, 2000, doi: https://doi.org/10.1002/1096-9918(200006)29:6<403::AID-SIA884>3.0.CO;2-8.

[24] I. M. Band, Yu. I. Kharitonov, and M. B. Trzhaskovskaya, "Photoionization cross sections and photoelectron angular distributions for x-ray line energies in the range 0.132–4.509 keV targets: $1 \leq Z \leq 100$," *At. Data Nucl. Data Tables*, vol. 23, no. 5, pp. 443–505, May 1979, doi: 10.1016/0092-640X(79)90027-5.

[25] sherena.johnson@nist.gov, "NIST Standard Reference Database 82," *NIST*, Aug. 27, 2010. https://www.nist.gov/srd/nist-standard-reference-database-82 (accessed Mar. 16, 2021).

[26] Y. Wang *et al.*, "Van der Waals contacts between three-dimensional metals and two-dimensional semiconductors," *Nature*, vol. 568, no. 7750, Art. no. 7750, Apr. 2019, doi: 10.1038/s41586-019-1052-3.

[27] L. A. Walsh *et al.*, "Interface Chemistry of Contact Metals and Ferromagnets on the Topological Insulator Bi_2Se_3," *J. Phys. Chem. C*, vol. 121, no. 42, pp. 23551–23563, Oct. 2017, doi: 10.1021/acs.jpcc.7b08480.

[28] C. D. Spataru and F. Léonard, "Fermi-level pinning, charge transfer, and relaxation of spin-momentum locking at metal contacts to topological insulators," *Phys. Rev. B*, vol. 90, no. 8, p. 085115, Aug. 2014, doi: 10.1103/PhysRevB.90.085115.

[29] S. Shriwastava and C. C. Tripathi, "Metal–Insulator–Metal Diodes: A Potential High Frequency Rectifier for Rectenna Application," *J. Electron. Mater.*, vol. 48, no. 5, pp. 2635–2652, May 2019, doi: 10.1007/s11664-018-06887-9.